INTERNATIONAL JOURNAL FOR NUMERICAL METHODS IN FLUIDS
Int. J. Numer. Meth. Fluids **29**: 159–191 (1999)

COMPACT FINITE DIFFERENCE SCHEMES ON NON-UNIFORM MESHES. APPLICATION TO DIRECT NUMERICAL SIMULATIONS OF COMPRESSIBLE FLOWS

L. GAMET[a,*], F. DUCROS[b], F. NICOUD[b] AND T. POINSOT[b,c]

[a] *CRCT/Institut Français du Pétrole, 1 Av. de Bois Préau, 92852 Rueil-Malmaison Cedex, France*
[b] *CRCT/CERFACS, 42 Av. G. Coriolis, 31057 Toulouse Cedex, France*
[c] *CRCT/IMFT, Av. C. Soula, 31400 Toulouse Cedex, France*

SUMMARY

In this paper, the development of a fourth- (respectively third-) order compact scheme for the approximation of first (respectively second) derivatives on non-uniform meshes is studied. A full inclusion of metrics in the coefficients of the compact scheme is proposed, instead of methods using Jacobian transformation.

In the second part, an analysis of the numerical scheme is presented. A numerical analysis of truncation errors, a Fourier analysis completed by stability calculations in terms of both semi- and fully discrete eigenvalue problems are presented. In those eigenvalue problems, the pure convection equation for the first derivative, and the pure diffusion equation for the second derivative are considered.

The last part of this paper is dedicated to an application of the numerical method to the simulation of a compressible flow requiring variable mesh size: the direct numerical simulation of compressible turbulent channel flow. Present results are compared with both experimental and other numerical (DNS) data in the literature. The effects of compressibility and acoustic waves on the turbulent flow structure are discussed. Copyright © 1999 John Wiley & Sons, Ltd.

KEY WORDS: compact scheme/compact differencing; non-uniform meshes; finite difference; compressible; turbulent channel flow

1. INTRODUCTION

Direct numerical simulations (DNS) have become one of the major tools to study and model turbulent flows [1–7]. Even though these techniques demonstrated high accuracy in many flows, their application has been often limited to simple geometries (cubes), using simplified Navier–Stokes equations (incompressible flows), low Reynolds numbers and high-order numerical techniques (spectral methods). Extending DNS to more complex flows, more complex physics or higher Reynolds numbers, requires further improvements of DNS tools. The ‘high Reynolds’ objective is of course the central point in large-eddy simulations (LES) techniques, which are beyond the focus of this paper. It is clear, however, that LES raise specific difficulties in terms of numerical methods [8–10], but they will also have to be performed using compressible formulations in many cases.

---

[*] Correspondence to: CRCT/Institut Français du Pétrole, 1 Av. de Bois Préau, 92852 Rueil-Malmaison Cedex, France.

CCC 0271–2091/99/020159–33$17.50

Received September 1997
Revised January 1998

The objectives of this paper are the following:

- To develop a high-order compact finite difference method able to handle variable grid sizes. Compact schemes on regular meshes have been used extensively as a substitute for spectral techniques [3,4,11], but their extension to irregular meshes, e.g. to study near-wall turbulence, is not straightforward. It will be discussed here in terms of theory, linear stability, analysis and precision. Two methods to perform derivative computations on variable grids will be presented and discussed.
- To perform a direct numerical simulation of a channel flow using a fully compressible code. The channel flow is one of the best documented test cases to validate a DNS or a LES code. However, computing this flow with a compressible code requires the proper handling of acoustic waves. For channel flow geometries, acoustic waves are trapped in the computational box and may interact in complex ways with the turbulent flow, making the present test difficult to use. It will be shown that, for usual DNS conditions, the second acoustic transverse mode is excited by turbulence, but that it has a negligible effect on turbulence statistics.

2. COMPACT SCHEME ON STRETCHED GRIDS

2.1. Compact scheme on uniform meshes

Lele [11] recently proposed a generalization of the classical Padé schemes. The schemes discussed in [11] represent a family of high-order finite difference compact schemes, which can be used not only for the evaluation of derivatives, but also for filtering and interpolation applications. Algorithms based on such schemes can provide numerical solutions with spectral-like resolution and very low numerical dissipation.

Consider a one-dimensional mesh with node co-ordinates x_i, where $1 \leq i \leq N$ is the node index, and a function with given values $f_i = f(x_i)$ at the nodes. In this paragraph, a uniform mesh with equal nodes spacings $h = x_i - x_{i-1}$ will first be considered. A sixth-order tridiagonal approximation f'_i of the first derivative $(\mathrm{d}f/\mathrm{d}x)_{(x_i)}$ can then be obtained, with (see scheme 2.1.7 of [11]):

$$\frac{1}{3} f'_{i-1} + f'_i + \frac{1}{3} f'_{i+1} = \frac{14}{9} \frac{f_{i+1} - f_{i-1}}{2h} + \frac{1}{9} \frac{f_{i+2} - f_{i-2}}{4h}. \tag{2.1}$$

Similarly, a sixth-order tridiagonal approximation f''_i of the second derivative $(\mathrm{d}^2 f/\mathrm{d}x^2)_{(x_i)}$ is given by (see scheme 2.2.7 of [11]):

$$\frac{2}{11} f''_{i-1} + f''_i + \frac{2}{11} f''_{i+1} = \frac{12}{11} \frac{f_{i+1} - 2f_i + f_{i-1}}{h^2} + \frac{3}{11} \frac{f_{i+2} - 2f_i + f_{i-2}}{4h^2}. \tag{2.2}$$

For non-periodic boundary problems, non-centered boundary schemes are required at points close to the boundaries, i.e. at nodes 1, 2, $N-1$ and N. Classical fourth-order Padé schemes and third-order compact relations can be used respectively, at nodes 2 and $N-1$ and at nodes 1 and N [11] for both derivatives. In practice, the boundary formulation at nodes 1 and 2 for the first derivative is given by:

$$\begin{aligned} i=1,&\quad f'_1 + 2f'_2 = \frac{1}{h}\left(-\frac{5}{2}f_1 + 2f_2 + \frac{1}{2}f_3\right)\\ i=2,&\quad \frac{1}{4}f'_1 + f'_2 + \frac{1}{4}f'_3 = \frac{3}{4h}(f_3 - f_1) \end{aligned} \tag{2.3}$$

with similar relations at nodes $N-1$ and N; while the boundary formulation for the second derivative is taken under the form:

$$\begin{aligned} i=1,&\quad f''_1 + 11f''_2 = \frac{1}{h^2}(13f_1 - 27f_2 + 15f_3 - f_4)\\ i=2,&\quad \frac{1}{10}f''_1 + f''_2 + \frac{1}{10}f''_3 = \frac{6}{5h^2}(f_3 - 2f_2 + f_1) \end{aligned} \tag{2.4}$$

with similar relations at nodes $N-1$ and N.

2.2. Compact scheme on non-uniform meshes

Two formal methods can be used to generalize the application of the former compact finite difference scheme to non-uniform meshes. In a first approach, a Jacobian transformation (JT) can be applied, by defining transformed co-ordinates. Even though this method is used in most

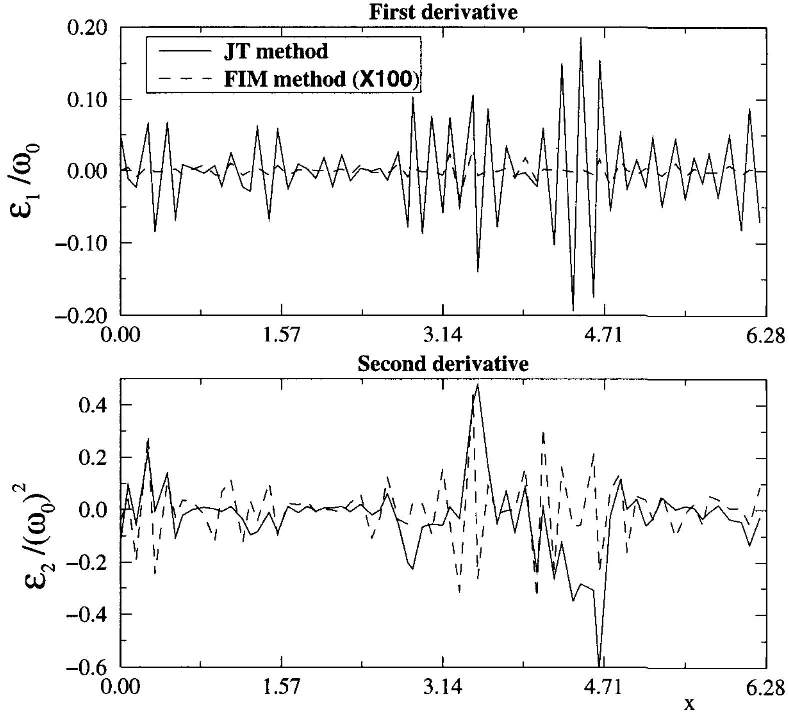

Figure 1. Comparison between the JT and FIM methods, on the first and second spatial derivatives errors of a cosine function.

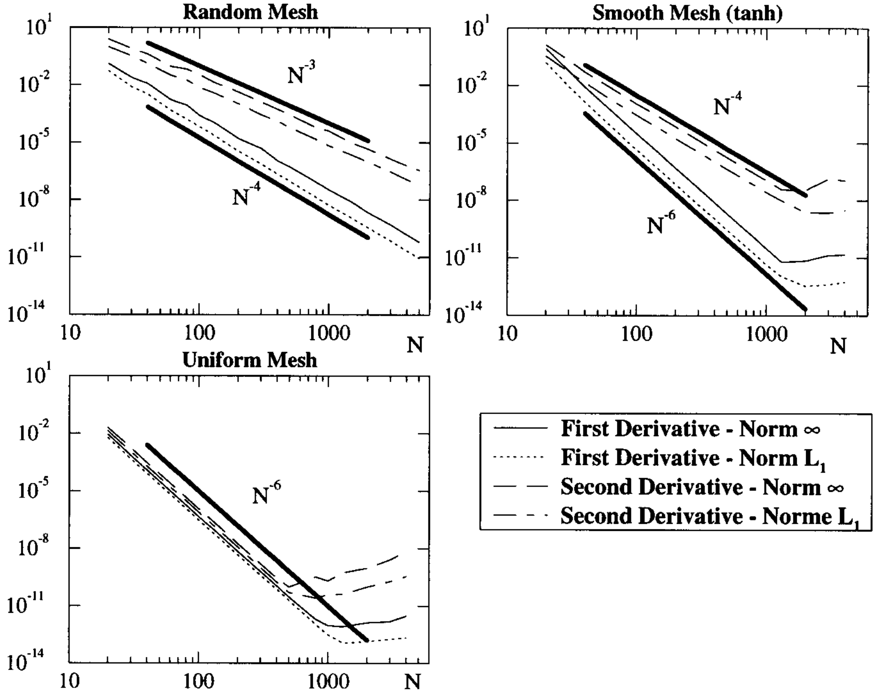

Figure 2. Norms of the truncation errors as a function of the number of nodes for three different meshes.

codes using curvilinear co-ordinates for steady flows, it is not a common choice for unsteady flows or for DNS (see Moin *et al.* [4]). A second technique called fully integrated metrics (FIM) consists of computing the derivatives directly on the irregular mesh. Below, it will be seen that the Jacobian transformation can lead to large errors in the case of non-smoothly varying mesh spacings. As a matter of fact, the accuracy of the numerical approximation can be maintained in the general case *only* for finite difference schemes that take into account the stretching of the grid.

2.2.1. Jacobian transformation. An extension of finite difference methods originally designed on uniform meshes can be obtained with the following simple relations:

$$\frac{\mathrm{d}f}{\mathrm{d}x}=\frac{\mathrm{d}f/\mathrm{d}\xi}{\mathrm{d}x/\mathrm{d}\xi}, \qquad \frac{\mathrm{d}^2f}{\mathrm{d}x^2}=\frac{\dfrac{\mathrm{d}^2f}{\mathrm{d}\xi}-\dfrac{\mathrm{d}f}{\mathrm{d}x}\dfrac{\mathrm{d}^2x}{\mathrm{d}\xi^2}}{\left(\dfrac{\mathrm{d}x}{\mathrm{d}\xi}\right)^2}. \tag{2.5}$$

This formulation involves defining the mesh transformation $\xi=\xi(x)$. Each of the derivatives on the right-hand side of Equation (2.5) can be evaluated using the finite difference scheme of Section 2.1. The essential assumption of this method is that the mesh must be sufficiently smooth so that $\mathrm{d}x/\mathrm{d}\xi$ and $\mathrm{d}^2x/\mathrm{d}\xi^2$ can be defined, and, in practice, calculated without appreciable loss in the overall accuracy.

2.2.2. Fully included metrics. An other method to treat non-uniform meshes is to directly include the metrics in the coefficients of the compact derivatives matrices. In this case, the compact schemes originally designed for uniform meshes must be adapted. The main constraint imposed is that the obtained scheme for non-uniform meshes must reduce exactly to the scheme for uniform meshes (presented in Section 2.1), in the case of a uniformly spaced grid.

2.2.2.1. First derivative approximation. For an irregular mesh, the approximation to the first derivative may be rewritten in a more general way:

$$\alpha_i f'_{i-1} + f'_i + \beta_i f'_{i+1} = A_i f_{i+1} + B_i f_{i-1} + C_i f_{i+2} + D_i f_{i-2} + E_i f_i, \tag{2.6}$$

where the coefficients α_i, β_i, A_i, B_i, C_i, D_i and E_i are functions of the non-uniform mesh spacings $h_k = x_k - x_{k-1}$. Following Lele [11], relations between the former coefficients can be derived by matching the Taylor series of various orders. The truncation error of the resulting scheme is determined by the first unmatched coefficient in the Taylor series. Here, the following relations are obtained:

$$\begin{aligned}
&A_i + B_i + C_i + D_i + E_i = 0 \quad \text{(order 0)}\\
&h_{i+1}A_i - h_i B_i + (h_{i+2} + h_{i+1})C_i - (h_i + h_{i-1})D_i = 1 + \alpha_i + \beta_i \quad \text{(order 1)}\\
&h^2_{i+1}A_i + h^2_i B_i + (h_{i+2} + h_{i+1})^2 C_i + (h_i + h_{i-1})^2 D_i = \frac{2!}{1!}(h_{i+1}\beta_i - h_i\alpha_i) \quad \text{(order 2)}\\
&h^3_{i+1}A_i - h^3_i B_i + (h_{i+2} + h_{i+1})^3 C_i - (h_i + h_{i-1})^3 D_i = \frac{3!}{2!}(h^2_{i+1}\beta_i + h^2_i\alpha_i) \quad \text{(order 3)}\\
&h^4_{i+1}A_i + h^4_i B_i + (h_{i+2} + h_{i+1})^4 C_i + (h_i + h_{i-1})^4 D_i = \frac{4!}{3!}(h^3_{i+1}\beta_i - h^3_i\alpha_i) \quad \text{(order 4)}\\
&h^5_{i+1}A_i - h^5_i B_i + (h_{i+2} + h_{i+1})^5 C_i - (h_i + h_{i-1})^5 D_i = \frac{5!}{4!}(h^4_{i+1}\beta_i + h^4_i\alpha_i) \quad \text{(order 5)}\\
&h^6_{i+1}A_i + h^6_i B_i + (h_{i+2} + h_{i+1})^6 C_i + (h_i + h_{i-1})^6 D_i = \frac{6!}{5!}(h^5_{i+1}\beta_i - h^5_i\alpha_i) \quad \text{(order 6)}
\end{aligned} \tag{2.7}$$

It was decided to limit this paper to a forth-order scheme[1]. The solution is then given in terms of a linear system of the first five equations in (2.7), where A_i, B_i, C_i, D_i and E_i are the

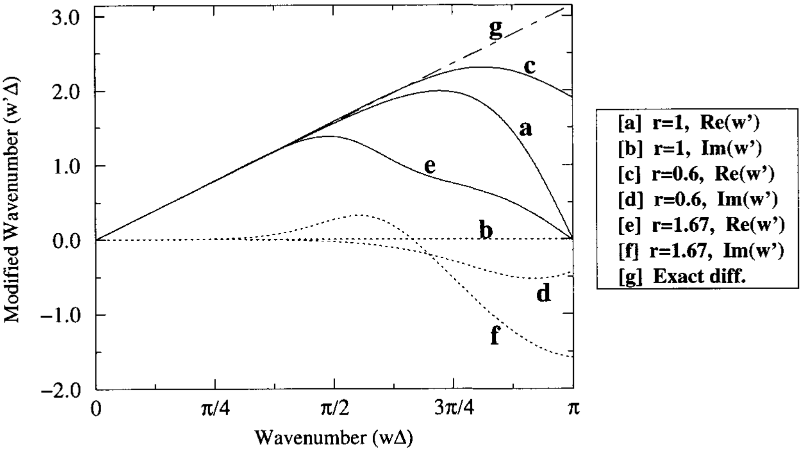

Figure 3. Modified wavenumber vs. wavenumber for the first derivative approximation. Plot shows real and imaginary part of w' for three different meshes: $r = 1$, uniform grid; $r = 0.6$, increasingly fine grid; $r = 1.67$, increasingly coarse grid.

---

[1] The precise characteristics of the scheme with highest formal accuracy (i.e. sixth-order) that can be obtained with Equations (2.7) are not addressed in this paper.

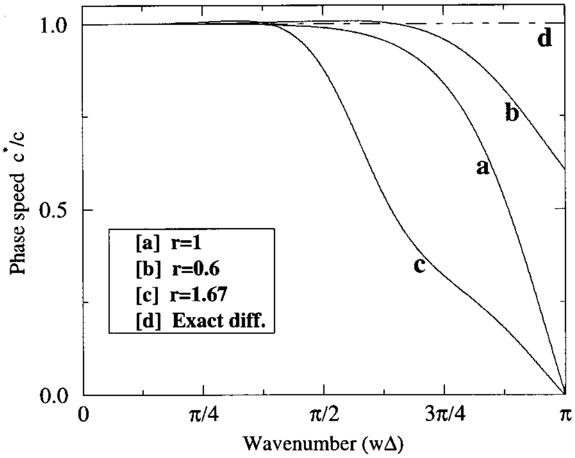

Figure 4. Phase speed vs. wavenumber for the first derivative approximation.

unknowns. This leads to the general expressions shown in Appendix A. In these expressions, the right-hand side parameters α_i and β_i are considered constants, equal to their value for uniform meshes, i.e. $\alpha_i = \beta_i = 1/3$. Thus, the final scheme for the first derivative will reduce exactly to the scheme in Section 2.1, in the case of a uniformly spaced grid. For sufficiently smooth grids, this scheme can gain up to two orders of accuracy. For grids where the spacing does not vary smoothly, fourth-order accuracy will still be obtained. The leading truncation error term can formally be written as:

$$\epsilon_1 = \left[h_{i+1}^5 A_i - h_i^5 B_i + (h_{i+2} + h_{i+1})^5 C_i - (h_i + h_{i-1})^5 D_i - \frac{5!}{4!}(h_{i+1}^4 \beta_i + h_i^4 \alpha_i) \right] \frac{f_i^{(5)}}{5!} \tag{2.8}$$

and is of the order $O(h_i^4)$.

For non-periodic boundaries, Equation (2.6) can no longer be applied to points close to the boundary, so that boundary schemes at nodes 1, 2, $N-1$ and N are required. The first derivative at boundary point $i = 1$ is calculated from:

$$f'_1 + \alpha f'_2 = Af_1 + Bf_2 + Cf_3. \tag{2.9}$$

This relation can formally be third-order. A solution in terms of α, A, B and C is shown in Appendix B. At boundary point $i = 2$, the first derivative is obtained from the relation:

$$\alpha f'_1 + f'_2 + \beta f'_3 = Af_1 + Bf_2 + Cf_3. \tag{2.10}$$

This relation can formally be fourth-order. The solution coefficients are shown in Appendix B.

2.2.2.2. Second derivative approximation. Similarly, the approximation to the second derivative is rewritten under the form:

$$\alpha_i f''_{i-1} + f''_i + \beta_i f''_{i+1} = A_i f_{i+1} + B_i f_{i-1} + C_i f_{i+2} + D_i f_{i-2} + E_i f_i. \tag{2.11}$$

Matching the Taylor series coefficients, the second set of unknowns α_i, β_i, A_i, B_i, C_i, D_i and E_i is the solution of the system:

$$A_i + B_i + C_i + D_i + E_i = 0 \quad \text{(order } -1\text{)}$$

$$h_{i+1} A_i - h_i B_i + (h_{i+2} + h_{i+1}) C_i - (h_i + h_{i-1}) D_i = 0 \quad \text{(order 0)}$$

$$h_{i+1}^2 A_i + h_i^2 B_i + (h_{i+2} + h_{i+1})^2 C_i + (h_i + h_{i-1})^2 D_i = \frac{2!}{0!}(1 + \alpha_i + \beta_i) \quad \text{(order 1)}$$

$$\begin{aligned}
&h_{i+1}^3 A_i - h_i^3 B_i + (h_{i+2}+h_{i+1})^3 C_i - (h_i+h_{i-1})^3 D_i = \frac{3!}{1!}(h_{i+1}\beta_i - h_i\alpha_i) \quad \text{(order 2)}\\
&h_{i+1}^4 A_i + h_i^4 B_i + (h_{i+2}+h_{i+1})^4 C_i + (h_i+h_{i-1})^4 D_i = \frac{4!}{2!}(h_{i+1}^2\beta_i + h_i^2\alpha_i) \quad \text{(order 3)}\\
&h_{i+1}^5 A_i - h_i^5 B_i + (h_{i+2}+h_{i+1})^5 C_i - (h_i+h_{i-1})^5 D_i = \frac{5!}{3!}(h_{i+1}^3\beta_i - h_i^3\alpha_i) \quad \text{(order 4)}\\
&h_{i+1}^6 A_i + h_i^6 B_i + (h_{i+2}+h_{i+1})^6 C_i + (h_i+h_{i-1})^6 D_i = \frac{6!}{4!}(h_{i+1}^4\beta_i + h_i^4\alpha_i) \quad \text{(order 5)}
\end{aligned} \tag{2.12}$$

Here, it was decided to limit this paper to a third-order scheme. The general solution shown in Appendix A is given in terms of a linear system of the five first equations in (2.12), where A_i, B_i, C_i, D_i and E_i are the unknowns. As in the first derivative case, the parameters α_i and β_i are considered constants, equal to their value for uniform meshes, i.e. $\alpha_i = \beta_i = 2/11$. The final scheme for the second derivative will reduce exactly to the scheme given by Equation (2.2), for uniformly spaced grids. The leading truncation error term for the second derivative approximation can formally be written as:

$$\epsilon_2 = \left[h_{i+1}^5 A_i - h_i^5 B_i + (h_{i+2}+h_{i+1})^5 C_i - (h_i+h_{i-1})^5 D_i - \frac{5!}{3!}(h_{i+1}^3\beta_i - h_i^3\alpha_i) \right] \frac{f_i^{(5)}}{5!} \tag{2.13}$$

and is of order $O(h_i^3)$.

For non-periodic boundaries, Equation (2.11) is no longer valid at nodes 1, 2, $N-1$ and N. The second derivative at boundary point $i=1$ is then calculated from:

$$f_1'' + \alpha f_2'' = Af_1 + Bf_2 + Cf_3 + Df_4. \tag{2.14}$$

If α is considered a parameter, this relation can formally be second-order. Solutions for A, B, C, D are shown in Appendix B. At boundary point $i=2$, the second derivative is obtained from the relation:

$$\alpha f_1'' + f_2'' + \beta f_3'' = Af_1 + Bf_2 + Cf_3 + Df_4. \tag{2.15}$$

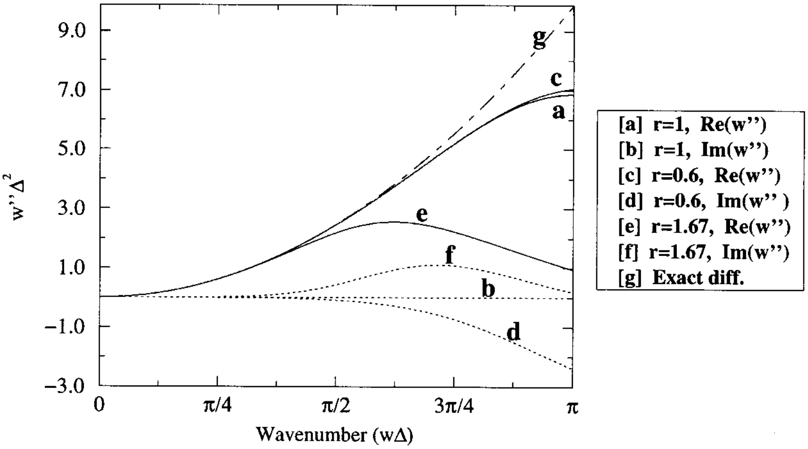

Figure 5. Modified wavenumber vs. wavenumber for the second derivative approximation. Plot shows real and imaginary part of w'' for three different meshes: $r=1$, uniform grid; $r=0.6$, increasingly fine grid; $r=1.67$, increasingly coarse grid.

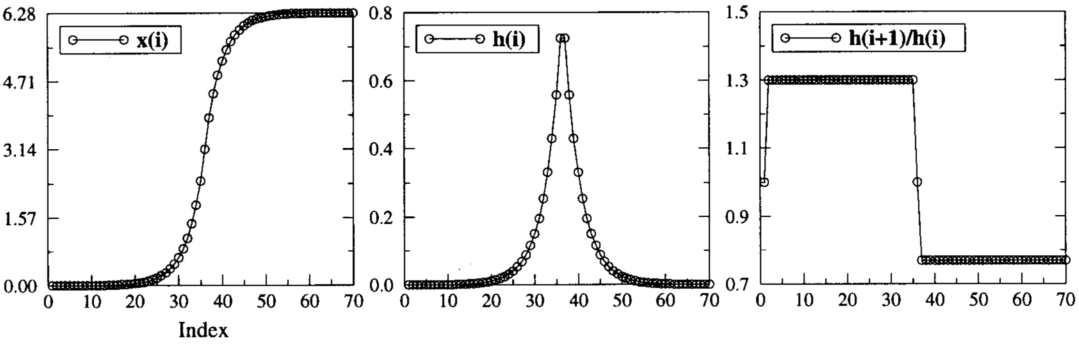

(a) Piecewise Geometric mesh

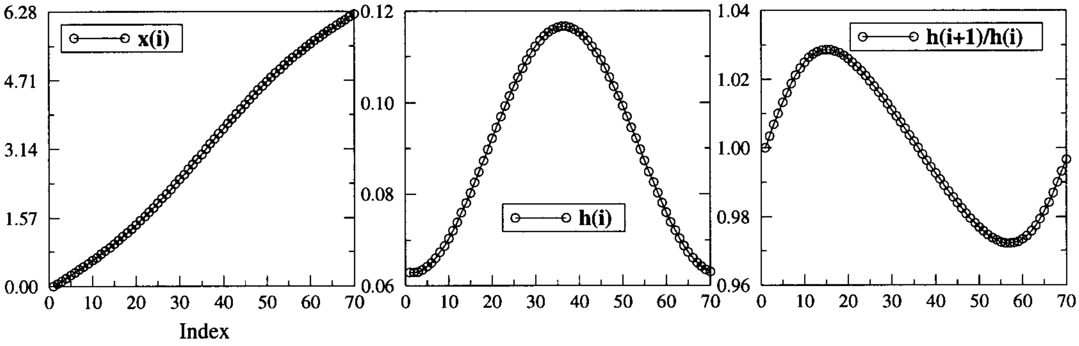

(b) Cosine-based mesh

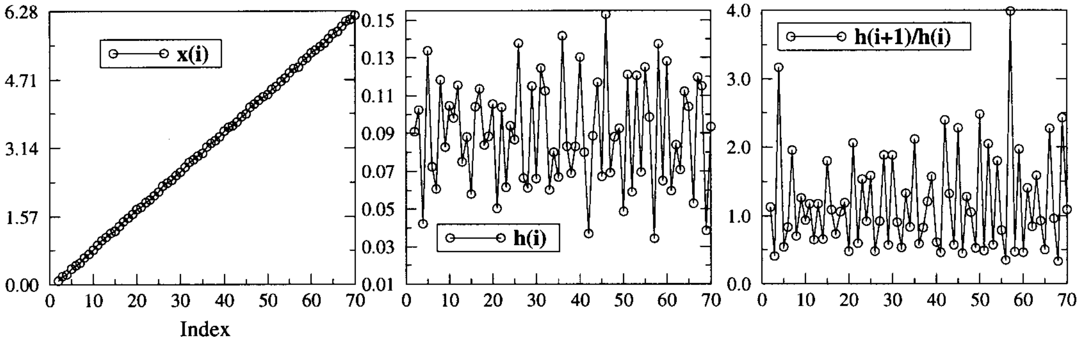

(c) Random mesh

Figure 6. Characteristics of non-uniform grids used in semi- and fully-discrete eigenvalues problems.

If α and β are considered parameters, this relation can formally be second-order. Solutions for A, B, C, D are shown in Appendix B.

2.2.3. Preliminary result. In a first approach, a simple comparison is made between the JT method using transformed co-ordinates, and the FIM method with inclusion of metrics in the compact matrix. As already stated, the FIM method might produce less error than the JT method in the case of non-smoothly varying meshes.

As an example of a non-smoothly varying mesh, a 70-points one-dimensional periodic non-uniform mesh of random type is chosen, on a domain of size $L_x = 2\pi$, with node co-ordinates given by:

$$x_i = (i - 1 + C\zeta_{\text{rnd}})h \tag{2.16}$$

ζ_{rnd}, with $-1 \leq \zeta_{\text{rnd}} \leq 1$, are random numbers and C is a constant taken as $C = 0.3$; h is the equal mesh spacing obtained for $C = 0$. For this particular mesh, the maximum theoretical stretching factor between two successive cells is $(1 + 2C)/(1 - 2C)$, and takes the value of 4.0. This mesh clearly does not satisfy regularity conditions required for the JT method. However, it is representative of grids which will have to be used for DNS or LES of complex geometries, where the mesh can become (especially in 3D) quite irregular.

The first and second derivatives of a known periodic cosine function $f = \cos(\omega_0 x + \phi_0)$ are calculated using both methods on the previous domain (chosen here as $\omega_0 = 4$ and $\phi_0 = 1$). Errors between the analytical and numerical derivatives, ($\epsilon = f^{(k)} - f^{(k)\text{analytical}}$ are calculated over the 1D domain. The errors are normalized by ω_0^k, with $k = 1$ (respectively $k = 2$) for the first (respectively second) derivative, and are shown in Figure 1. In Figure 1, the FIM method errors are multiplied by a scaling factor of 100. Much larger errors are obtained with the JT method.

As a conclusion, in the case of a non-sufficiently smooth mesh, the classical JT method using transformed co-ordinates can lead to larger errors. So in general, the JT method should be used very carefully and obviously eliminated in cases like the one shown here. In the following, only the FIM method will be studied.

2.3. Analysis of the resolution characteristics

In this section, the general characteristics of the compact scheme with fully included metrics for non-uniform meshes are described.

2.3.1. Truncation errors and order. The formal leading truncation error terms for the first (ϵ_1) and second derivative (ϵ_2) approximations are given by Equations (2.8) and (2.13) respectively, showing that the compact scheme with fully included metrics is formally fourth- and third-order respectively.

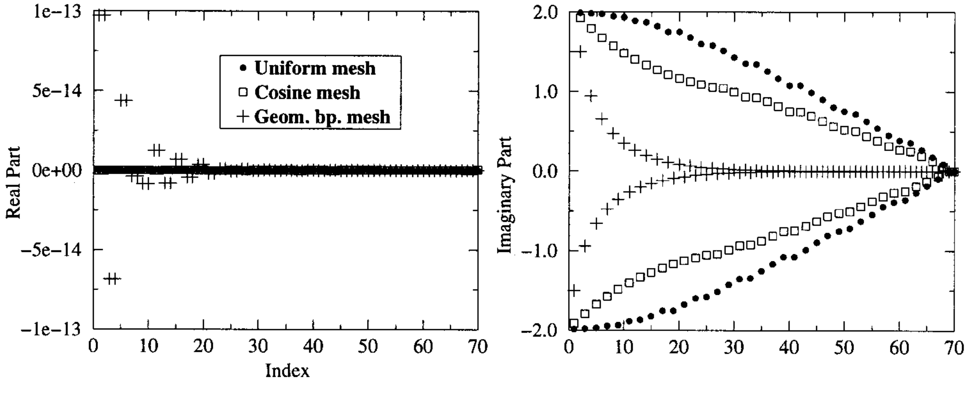

Figure 7. Eigenvalue spectrum for the semi-discrete case in a periodic domain, considering the constant speed advection problem (spatial first derivative).

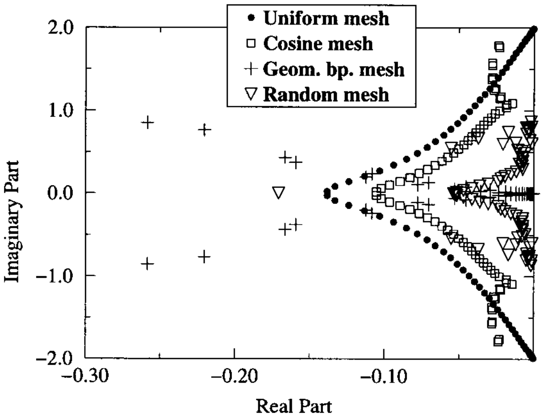

Figure 8. Eigenvalue spectrum for the semi-discrete case in a non-periodic domain, considering the constant speed advection problem (spatial first derivative).

Numerical calculations of the truncation errors of the derivatives can also provide a good estimate of the order of the scheme. The idea consists of calculating the numerical first and second derivatives of an analytical function with known derivatives. The chosen function is a cosine function (the same as in Section 2.2.3) over a periodic domain of length $L_x = 2\pi$. Then the norms (see Equation (2.17) below) of the error ϵ_k between the analytical and numerical derivatives can be estimated. The following notations will be used:

$$\|\epsilon_k\|_\infty = \max_{1\le i\le N} \left|f_i^{(k)} - f_i^{(k)\text{analytical}}\right|,$$
$$\|\epsilon_k\|_{\mathscr{L}_1} = \frac{1}{N}\sum_{i=1}^{N} \left|f_i^{(k)} - f_i^{(k)\text{analytical}}\right|. \tag{2.17}$$

Numerical tests were conducted on three different types of meshes, on a periodic domain of length $L_x = 2\pi$: a uniform mesh, a random mesh (see Equation (2.16)), and a smoothly varying mesh based on hyperbolic functions defined by:

$$x_i = \frac{L_x}{2}\,[1 + C\tanh(K\eta_i)] \quad \begin{array}{ll} \text{with} & K = \operatorname{Argtanh}\left(\dfrac{1}{C}\right), \\ \text{and} & -1 \le \eta_i = 2\dfrac{i-1}{N-1} - 1 \le +1. \end{array} \tag{2.18}$$

The constants in the random and hyperbolic tangent meshes definitions are respectively, 0.3 and 1.05.

The $\|\epsilon_k\|_\infty$ and $\|\epsilon_k\|_{\mathscr{L}_1}$ norms of the calculated truncation errors as a function of the number of nodes for three different meshes are shown in Figure 2. Thus, it is verified that a sixth-order scheme is recovered in the case of a uniform mesh. As expected, a fourth-order scheme on f' (third on f'') is found in the general case (random mesh). However, in the case of a smoothly varying mesh, the general expected orders are improved. In the tanh mesh example of Figure 2, the scheme is of sixth-order (respectively fourth-order) for the first (respectively second) derivative. The raise at high N on some error curves of Figure 2 is due to numerical machine precision, and can be highly machine-dependent.

2.3.2. Fourier analysis of error. Additional information about the behavior of numerical schemes can be obtained with Fourier analysis (see Lele [11], Vitchenevsky and Bowles [12] and Cain and Bush [13] for stretched grids).

Consider a Fourier mode in space:

$$f(x) = \mathrm{e}^{jwx}, \tag{2.19}$$

where $j = \sqrt{-1}$. The exact first derivative of this function with respect to x is $\partial f/\partial x = jwf$. If $\delta f/\delta x$ represents the numerical approximation of the first derivative of f using the FIM method, the 'modified wave number' $w'(w)$ can be defined by:

$$\frac{\delta f}{\delta x} = jw'f = jw'\,\mathrm{e}^{jwx}. \tag{2.20}$$

Exact differentiation corresponds to $w'(w) = w$. The difference between $w'(w)$ and w is then a measure of error in the first derivative approximation.

If the second derivative scheme is considered, the exact second derivative of f will be $\partial^2 f/\partial x^2 = -w^2 f$, while the numerical approximation of the second derivative can be written in the form:

$$\frac{\delta^2 f}{\delta x^2} = -w''f. \tag{2.21}$$

The difference between $w''(w)$ and w^2 is a measure of error in the second derivative approximation.

2.3.2.1. Fourier analysis for the first derivative. The effects of grid non-uniformity are examined by considering a simple stretched grid given by:

$$x_i = x_{i-1} + \Delta\, r^{i-2}. \tag{2.22}$$

Application of the former equation to the FIM method gives:

$$w'_i = -j\,\frac{A_i\,\mathrm{e}^{jwh_{i+1}} + B_i\,\mathrm{e}^{-jwh_i} + C_i\,\mathrm{e}^{jw(h_{i+1}+h_{i+2})} + D_i\,\mathrm{e}^{-jw(h_{i-1}+h_i)} + E_i}{1 + \alpha_i\,\mathrm{e}^{-jwh_i} + \beta_i\,\mathrm{e}^{jwh_{i+1}}}, \tag{2.23}$$

where the coefficients $\alpha_i = \beta_i = 1/3$, A_i, B_i, C_i, D_i and E_i are solutions of (2.7). Replacing $h_i = x_i - x_{i-1} = \Delta\, r^{i-2}$, and the coefficients by their respective values (see Appendix A) in the former equation, produces $w'_i(w)$ (not shown here).

Figure 3 shows the real and imaginary parts of $w'(w)\Delta$ plotted against $w\Delta$ for the FIM method and for three distinct mesh cases: $r = 1$, uniform grid; $r = 0.6$, increasingly fine grid; $r = 1.67$, increasingly coarse grid. It is to be noted that $w\Delta = \pi$ corresponds to the 2-δ wave, with two points per wavelength. From Figure 3, it can be seen that the real part of $w'(w)$ follows the exact differentiation (curve g) over a decreasing range of wavenumbers as r increases. In the uniform mesh case, $w'(w)$ is purely real, and the results presented in figure 2 of [11] are recovered. In the $r = 0.6$ case, $\Im(w'(w))$ is negative. On the other hand, $\Im(w'(w))$ is positive over a portion of the wavenumber domain for $r = 1.67$. From the observation that $\Im(w'(w)) > 0$, it is however, erroneous to conclude that the semi-discretized scheme is unstable. Stability considerations are studied in the next section using eigenvalues analysis.

If the constant speed advection equation is considered (see Equation (2.25) in the next section), it can be shown that (see Vitchenevsky and Bowles [12]) the phase speed of a wave of wavenumber w is given by $c^*/c = \Re(w')/w$. Figure 4 shows phase speed information for the first derivative. From this figure, it can be observed that the waves will propagate too slowly

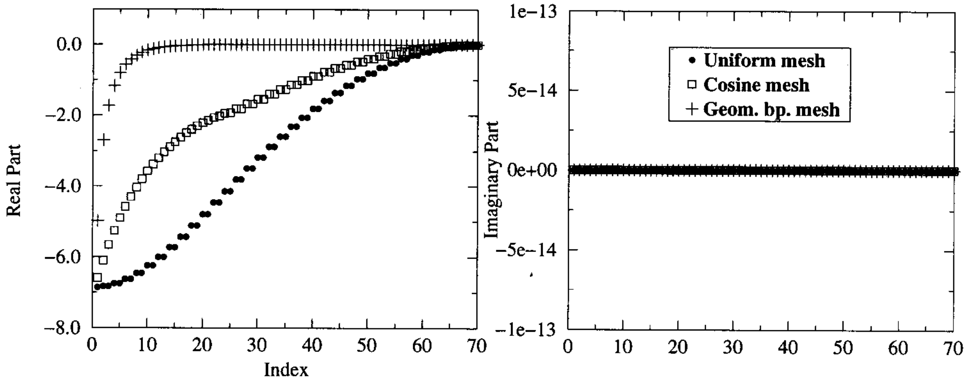

Figure 9. Eigenvalue spectrum for the semi-discrete case in a periodic domain, considering the pure diffusion problem (spatial second derivative).

for some values of $w\Delta$, and slightly too fast for some other values (in the cases of $r = 0.6$ and $r = 1.67$).

2.3.2.2. Fourier analysis for the second derivative. For the second derivative, the modified wavenumber can be written:

$$w_i'' = -j\,\frac{A_i\,e^{jwh_{i+1}} + B_i\,e^{-jwh_i} + C_i\,e^{jw(h_{i+1}+h_{i+2})} + D_i\,e^{-jw(h_{i-1}+h_i)} + E_i}{1 + \alpha_i\,e^{-jwh_i} + \beta_i\,e^{jwh_{i+1}}}, \tag{2.24}$$

where the coefficients $\alpha_i = \beta_i = 2/11$, A_i, B_i, C_i, D_i and E_i are solutions of (2.12).

Figure 5 shows the real and imaginary parts of $w''(w)\Delta$ plotted against $w\Delta$ for the FIM method and for the same mesh cases as in the first derivative case. $\Re(w''(w))$ follows the exact differentiation (curve g) over a decreasing range of wavenumbers as r increases. However, a slight difference is noticeable between the $\Re(w''(w))$ curves at $r = 1$ and $r = 0.6$. The same conclusions as in the first derivative case hold for positiveness of $\Im(w''(w))$.

2.3.3. Numerical analysis of stability. In this section, the general theory of the eigenvalue analysis of the complete semi-discretized or fully-discretized differencing scheme is firstly recalled. This type of analysis is then applied to the FIM method.

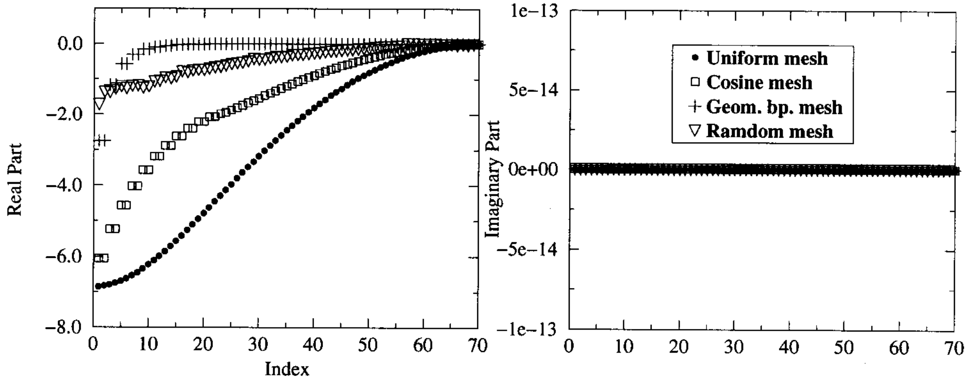

Figure 10. Eigenvalue spectrum for the semi-discrete case in a non-periodic domain, considering the pure diffusion problem (spatial second derivative).

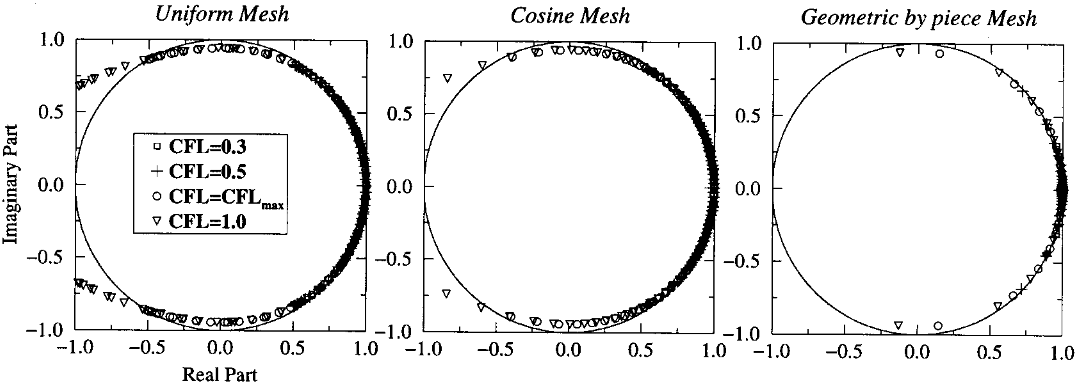

Figure 11. Eigenvalue spectrum for the fully-discrete case in a periodic domain, considering the constant speed advection problem (spatial first derivative and RK3 time advancement). Plots in the complex plane show also the unit circle.

2.3.3.1. Semi-discrete and fully-discrete eigenvalue problems for the first derivative. Consider the constant speed advection equation:

$$\frac{\partial f}{\partial t} + c\frac{\partial f}{\partial x} = 0, \tag{2.25}$$

over a one-dimensional periodic domain of length 2π, in the general case of a non-uniform mesh. The latter equation is to be completed by an initial value for the function, i.e. $f_{(x,t=0)}$. No particular boundary conditions are required on a periodic domain.

The spatial first derivative compact schemes for either uniform or non-uniform meshes can be formally written in a general matrix form, as:

$$\underline{\mathbf{A}}\hat{f}' = \underline{\mathbf{B}}\hat{f}, \tag{2.26}$$

where $\underline{\mathbf{A}}$ and $\underline{\mathbf{B}}$ are $N \times N$ square matrices, $\hat{f} = (f_i)_{1 \le i \le N}$ and $\hat{f}' = (f'_i)_{1 \le i \le N}$ are $N \times 1$ vectors representing the function and its derivative at the nodes.

Multiplying the advection equation (2.25) by $\underline{\mathbf{A}}$ gives:

$$\underline{\mathbf{A}}\frac{\partial \hat{f}}{\partial t} + c\underline{\mathbf{B}}\hat{f} = 0. \tag{2.27}$$

At this point, the time discretization problem has not been yet addressed, and the semi-discrete problem is considered (exact time advancement). Since the former set of equations is a linear system of ODEs in time (see Lele [11]), it is consistent to look for solutions in terms of normal modes, i.e. $\hat{f} = \exp(\omega t)\tilde{f}$. The system then reduces to the following eigenvalue problem:

$$-\frac{\omega h_{\min}}{c}\underline{\mathbf{A}}\tilde{f} = h_{\min}\underline{\mathbf{B}}\tilde{f}, \tag{2.28}$$

where $h_{\min} = \min_{1 \le i \le N} h_i$. A semi-discrete stability analysis can be obtained by analysing the eigenvalues, which are written under the reduced form $\omega' = \omega h_{\min}/c$. These eigenvalues are generally complex. For the numerical stability of the semi-discrete problem, these eigenvalues must lie in the left half of the complex plane.

To consider the full discretization scheme, time advancement must be addressed. In this paper, a third-order explicit Runge–Kutta method was chosen to advance the solution in time. The Runge–Kutta method may be written in the following manner for linear differential equations (see Vitchenevsky and Bowles [12]):

$$\hat{f}^{n+1} = \sum_{k=0}^{M} \frac{(\Delta t \cdot \underline{\mathscr{A}})^k}{k!} \hat{f}^n \quad M = 3 \quad \text{for} \quad \text{RK3}, \tag{2.29}$$

where $\hat{f}^n = (f_i^n)_{1 \leq i \leq N}$ is the $N \times 1$ vector of the variable at time n, and $\underline{\mathscr{A}}$ is the global spatial differentiation operator. Here, $\underline{\mathscr{A}} = \underline{\underline{\mathbf{A}}}^{-1}\underline{\underline{\mathbf{B}}}$, so that the final discretization for a RK3 time integration scheme may be written in the form:

$$\hat{f}^{n+1} = \sum_{k=0}^{3} \frac{(\lambda \cdot \underline{\underline{\mathbf{A}}}^{-1}\underline{\underline{\mathbf{B}}} h_{\min})^k}{k!} \hat{f}^n = \underline{\mathscr{K}} \hat{f}^n, \tag{2.30}$$

where $\lambda = c\Delta t / h_{\min}$ is the CFL number. Now, a stability analysis can be obtained by calculating the eigenvalues of the iteration matrix $\underline{\mathscr{K}}$. For the numerical stability of the fully-discrete problem, these eigenvalues must lie inside the unit circle in the complex plane.

2.3.3.2. Semi-discrete and fully-discrete eigenvalue problems for the second derivative. Similar relations can be established for the second spatial derivative by considering the pure diffusion equation on a periodic domain:

$$\frac{\partial f}{\partial t} = v \frac{\partial^2 f}{\partial x^2}. \tag{2.31}$$

The second derivative compact scheme can be written as $\underline{\underline{\mathbf{A}}}\hat{f}'' = \underline{\underline{\mathbf{B}}}\hat{f}$, so that it follows:

$$\underline{\underline{\mathbf{A}}} \frac{\partial \hat{f}}{\partial t} = v \underline{\underline{\mathbf{B}}} \hat{f}. \tag{2.32}$$

This paper also looks for solutions in the form $\hat{f} = \exp(\omega t)\tilde{f}$ and the resulting eigenvalue problem is:

$$\frac{\omega h_{\min}^2}{v} \underline{\underline{\mathbf{A}}} \tilde{f} = h_{\min}^2 \underline{\underline{\mathbf{B}}} \tilde{f}. \tag{2.33}$$

Eigenvalues (written as $\omega' = \omega h_{\min}^2 / v$) must lie in the left half of the complex plane for stability.

For the fully-discrete problem, with a RK3 time advancement scheme, the resulting eigenvalue problem reduces to

$$\hat{f}^{n+1} = \sum_{k=0}^{3} \frac{(Fo \cdot \underline{\underline{\mathbf{A}}}^{-1}\underline{\underline{\mathbf{B}}} h_{\min}^2)^k}{k!} \hat{f}^n = \underline{\underline{\mathscr{K}}} \hat{f}^n, \tag{2.34}$$

where $Fo = v\Delta t / h_{\min}^2$ is the Fourier number, and $\underline{\underline{\mathscr{K}}}$ represents the iteration matrix for the pure diffusion equation. In this second derivative case, it can be shown that both semi- and fully-discrete eigenvalues are real.

2.3.3.3. Non-periodic problems. If Equations (2.25) and (2.31) are considered over a non-periodic domain $[0, 2\pi]$, boundary conditions are to be supplied.

For the convection equation (2.25), and if $c > 0$, a physical boundary condition at $x = 0$ has to be prescribed in the form $f(x = 0, t) = g(t)$. Following Lele [11], and for stability analysis, there is only a slight loss of generality in assuming that $g(t) = 0$. For the diffusion equation (2.31), $f(x = 0, t) = 0$ and $f(x = L_x, t) = 0$ will be imposed.

In a non-periodic case, numerical boundary schemes for the compact scheme must be used on points close to the frontier. Boundary schemes presented in Section 2.2.2 are then used instead of the interior scheme. Moreover, in the numerical implementation of the above eigenvalue problems in the non-periodic case, the approximation of derivatives at boundary points is replaced by the imposed physical boundary condition.

2.3.3.4. Application to the FIM method. As an example, a 70-points 1D non-uniform mesh on a domain of size $L_x = 2\pi$ was chosen. An infinite variety of meshes could be used. As an example, uniform, piecewise geometric, cosine-based and random meshes will be considered in this section. The piecewise geometric mesh is a simple stretched grid in which each successive cell differs from the previous one by a factor r on the first half of the domain, and by a factor $1/r$ on the other half. The grid characteristics are shown in Figure 6(a), for $r = 1.3$. The cosine-based mesh is constructed with trigonometric functions according to:

$$x_i = \frac{L_x}{2}\left[1 + \eta_i + \frac{C-1}{\pi}\sin(\pi(\eta_i + 1))\right] \quad \text{with} \quad -1 \le \eta_i = 2\frac{i-1}{N-1} - 1 \le +1 \qquad (2.35)$$

in a periodic case. A smoothly varying mesh is obtained by choosing $C = 0.7$ (see Figure 6(b)). In practice, non-smooth grids with abrupt grid cell changes are only relevant in non-periodic problems. Also considered is the case of a random mesh (given by Equation (2.16) with a coefficient $C = 0.4$). This would be an example of the most severe case of non-smooth meshes that could be encountered in DNS or LES. Random grid characteristics are shown in Figure 6(c).

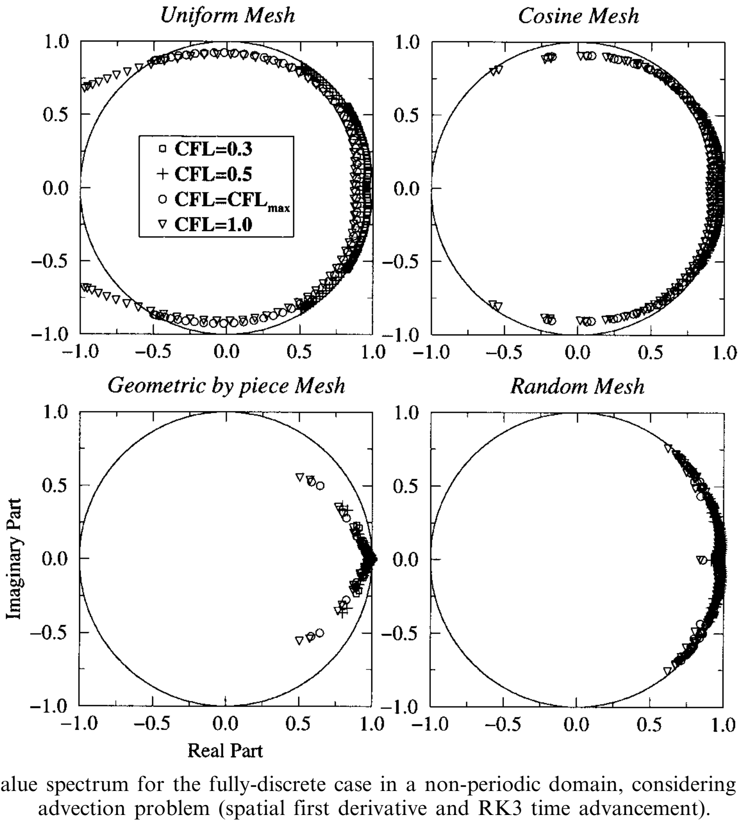

Figure 12. Eigenvalue spectrum for the fully-discrete case in a non-periodic domain, considering the constant speed advection problem (spatial first derivative and RK3 time advancement).

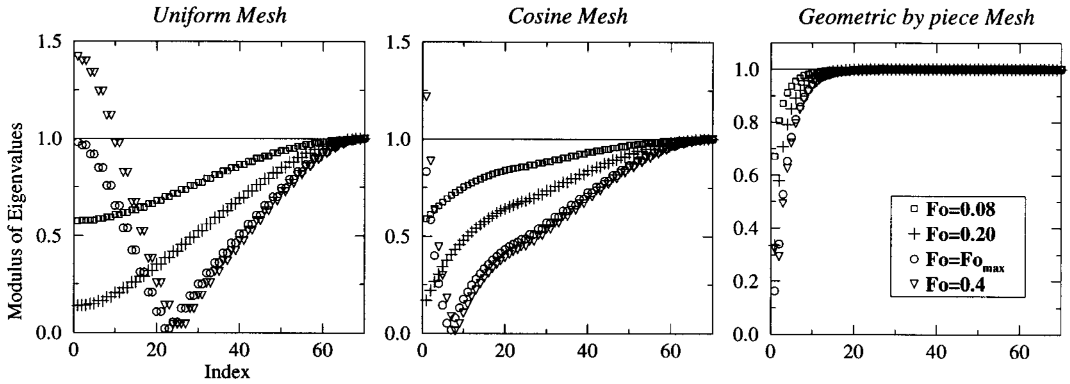

Figure 13. Eigenvalue spectrum for the fully-discrete case in a periodic domain, considering the pure diffusion problem (spatial second derivative and RK3 time advancement).

Calculated eigenvalues for the semi-discrete problem are shown in Figures 7 and 8 in the case of the pure convection equation (first derivative). In the periodic case, eigenvalues are purely imaginary. Their numerically calculated real part (using Matlab software) is of the order of machine precision, which can be seen on the left of Figure 7. In the non-periodic case, eigenvalues are complex. All eigenvalues lie in the left half of the complex plane.

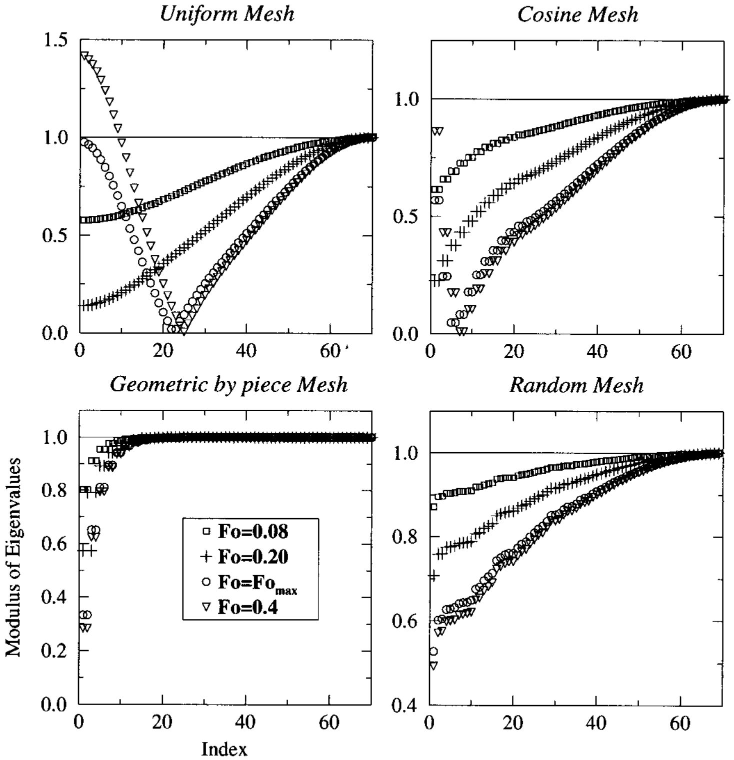

Figure 14. Eigenvalue spectrum for the fully-discrete case in a non-periodic domain, considering the pure diffusion problem (spatial second derivative and RK3 time advancement).

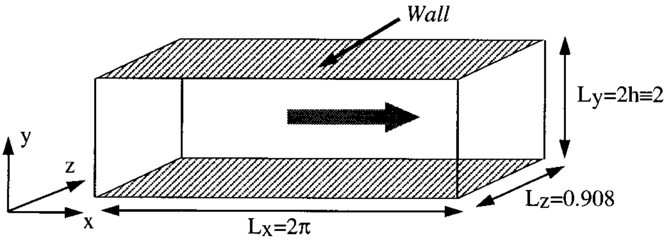

Figure 15. Geometry of the channel flow computational domain.

Eigenvalues for the semi-discrete problem for the diffusion equation (involving spatial second derivative) are plotted in Figures 9 and 10. Eigenvalues are real-valued for the diffusion equation case. The scheme also exhibits stable behavior for the semi-discrete case (eigenvalues with negative real part).

Figures 11 and 12 show the calculated eigenvalues for the fully-discrete problem (discretization in space and time) at different CFL numbers (where $\mathrm{CFL} = c\Delta t/h_{\min}$), and for the convection equation. $\mathrm{CFL}_{\max} \approx 0.8708$ is the stability limit obtained by Lele [11] in the case of a uniform mesh. In Figures 11 and 12, the eigenvalues are plotted in the complex plane for different types of meshes. All eigenvalues for CFL numbers less than $\mathrm{CFL}_{\max}$ lie inside the unit circle. In the non-uniform mesh cases, the CFL condition applies only at the smallest mesh spacing location, and is in fact a more restrictive condition. This could explain why, in a highly non-uniform mesh case (e.g. piecewise geometric or random in non-periodic cases), the scheme remains stable at CFL numbers as high as 1.

Figures 13 and 14 show the calculated eigenvalues in the diffusion equation case, for the fully-discrete problem (discretization in space and time), at different Fo. $Fo_{\max} \approx 0.3645$ is the

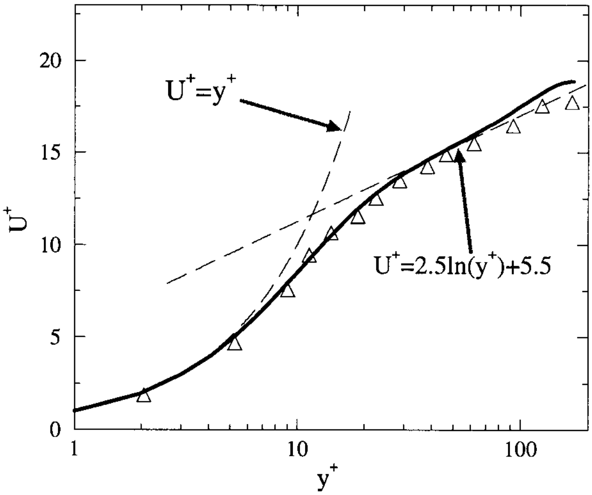

Figure 16. Mean streamwise velocity profile plotted in wall unit co-ordinates. Solid line shows present DNS results, and Δ symbols experimental data from Wei and Willmarth [17] at $Re_c = 2970$. The dashed line through the data is the 'law-of-the-wall' plot compiled by Coles [21,22] for a zero-pressure–gradient boundary layer.

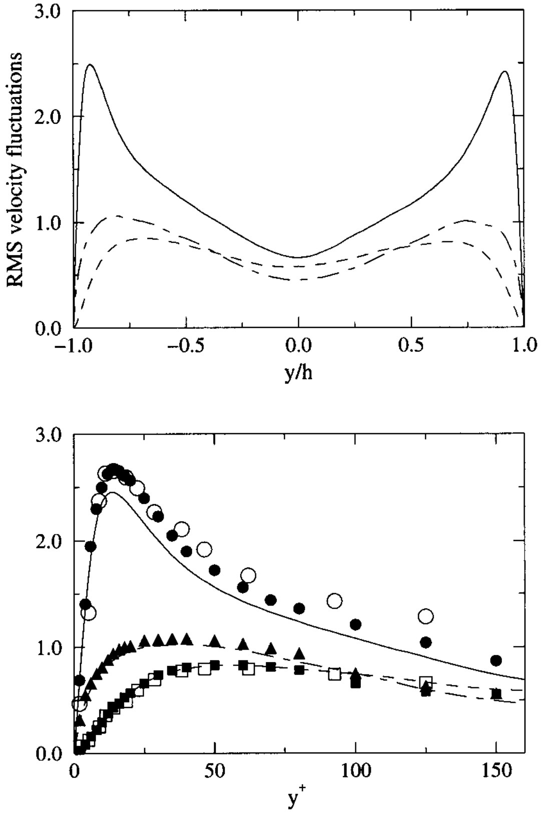

Figure 17. RMS velocity fluctuation normalized by the friction velocity. Top: in global co-ordinates; bottom: in wall co-ordinates. Open symbols represent experimental data from WW, solid symbols represent numerical data from KMM. Lines represent the current DNS results. —— and ●, u^+_{rms}; – – – and ▲, v^+_{rms}; --- and ■, w^+_{rms}. (Wei and Willmarth did not measure w_{rms}).

Fourier number stability limit discussed in Lele [11]. In these last figures, the calculated eigenvalues are real-valued. The periodic and non-periodic cases are similar and show a stable behavior.

In all cases, the FIM method exhibits no unstable eigenvalues for both semi- and fully-discrete problems, as long as stability criteria derived for regular meshes are fulfilled.

3. APPLICATION TO DIRECT NUMERICAL SIMULATIONS

This section shows an application of the FIM method to the simulation of a compressible flow requiring variable mesh size: the time-dependent turbulent flow in a periodic channel.

3.1. *Compressible flow equations*

The compressible turbulent flow of an ideal gas is governed by the full time-dependent Navier–Stokes equations (continuity, momentum and energy), written here in a conservative form:

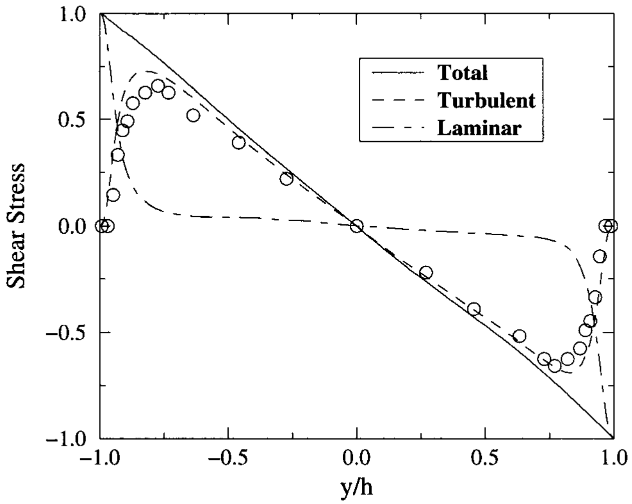

Figure 18. Mean shear stress profiles in global co-ordinates. ○ symbols represent WW turbulent shear stress experimental data.

$$
\begin{aligned}
&\frac{\partial \rho}{\partial t}+\frac{\partial(\rho u_i)}{\partial x_i}=0,\\
&\frac{\partial(\rho u_i)}{\partial t}+\frac{\partial(\rho u_i u_j)}{\partial x_j}+\frac{\partial p}{\partial x_i}=\frac{\partial \tau_{ij}}{\partial x_j},\\
&\frac{\partial \rho e_{\mathrm{t}}}{\partial t}+\frac{\partial}{\partial x_i}[(\rho e_{\mathrm{t}}+p)u_i]=\frac{\partial}{\partial x_i}(u_i\cdot\tau_{ij})-\frac{\partial q_i}{\partial x_i},
\end{aligned}
\tag{3.1}
$$

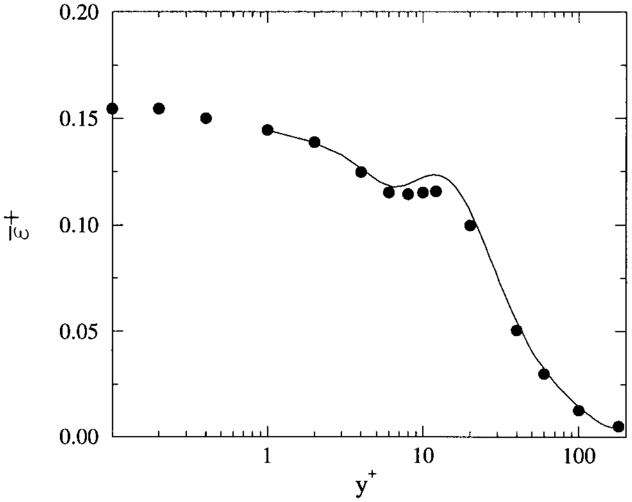

Figure 19. Distribution of $\bar{\varepsilon}^+$ in wall co-ordinates. Symbols (●) represent the numerical data of KMM.

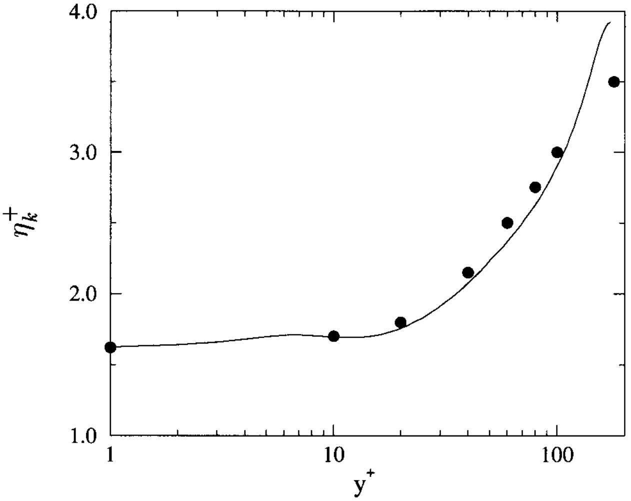

Figure 20. Kolmogorov microscale in wall units. Symbols (●) represent the numerical data of KMM.

where the viscous stress τ_{ij} is defined by:

$$\tau_{ij} = \mu\left(\frac{\partial u_i}{\partial x_j} + \frac{\partial u_j}{\partial x_i} - \frac{2}{3}\delta_{ij}\frac{\partial u_k}{\partial x_k}\right). \tag{3.2}$$

The heat flux q_j along x_j is related to temperature T by the Fourier law:

$$q_j = -k\frac{\partial T}{\partial x_j}. \tag{3.3}$$

The summation convention applies to repeated indices. Here ρ, p, u, v, w, e_t denote respectively, the density, pressure, fluid velocity components in the x-, y- and z-directions, and total energy per unit mass. The system must be supplemented with the definition of the total energy and the equation of state:

$$\rho e_t = \frac{p}{(\gamma - 1)} + \frac{1}{2}\rho(u^2 + v^2 + w^2) \tag{3.4}$$

and

$$p = \rho RT, \tag{3.5}$$

where $R = \mathscr{R}/\mathscr{M} = 287.15$ J kg^{-1} K^{-1}. $\mathscr{R}$ is the perfect gas constant and $\mathscr{M}$ is the molecular weight of the ideal gas.

The Reynolds number $Re_c = U_c h/\nu$ is introduced based on the centerline velocity U_c in the channel and on the channel half-width h. The Prandtl number is defined as $Pr = \mu C_p/k$, where k is the thermal conductivity and C_p the specific heat at constant pressure.

The Prandtl and Reynolds numbers, and the ratio of specific heats $\gamma = C_p/C_v$ are supposed constant. The dynamic and kinematic viscosities μ and ν are also supposed constant.

Finally, it should be noted that a skew-symmetric form of the non-linear terms in the Navier–Stokes equations is used to reduce aliasing errors (see Kravchenko and Moin [9] for more details).

3.2. Numerical conditions

In this section, a DNS of a turbulent periodic channel flow is described. Figure 15 shows a sketch of the computational geometry and of the co-ordinate system. Isothermal wall conditions are used at the top and bottom boundaries, while periodic boundary conditions are used in the streamwise (x) and spanwise (z) directions. Many experimental studies of developed turbulent channel flow can be found (Laufer [14], Comte-Bellot [15], Clark [16], Wei and Willmarth [17]). Many numerical studies concerning incompressible channel flow can also be found in the literature (Rai and Moin [4], Kim *et al.* [7], Moin and Kim [18], Antonia *et al.* [19]). Fewer studies are found for DNS of channel flows using a compressible formulation. In this paper, the aim is only to check the consistency of the results with other experimental/numerical studies, and to perform this simulation with a fully compressible code.

The channel half-width h is taken as the reference length. A computational domain of size $L_x = 2\pi h$, $L_y = 2h$ and $L_z = 0.908h$ in the three directions, is used. The x-, y- and z-co-ordinates belong to the intervals $0 \leq x \leq L_x$, $-L_y/2 \leq y \leq L_y/2$ and $0 \leq z \leq L_z$. According to Jimenez and Moin [20], a 'minimal channel flow' configuration can be computed to save CPU running time. They showed that for boxes wider than ≈ 100 wall units (see below) in the spanwise direction, the flow is turbulent and the low-order turbulence statistics are in good agreement with experiments. Similar results hold for the streamwise direction. The dimensions of the present calculation domain were chosen to respect the criteria of Jimenez and Moin [20].

Channel flow data are usually presented in wall units using normalized quantities defined by:

$$y^+ = \frac{\tilde{y} u_\tau}{\nu} \qquad u_i^+ = \frac{u_i}{u_\tau} \tag{3.6}$$

with

$$u_\tau = \sqrt{\frac{\tau_w}{\rho_w}} \quad \text{and} \quad \tau_w = \mu \left(\frac{\partial \bar{u}}{\partial y} \right)_{y=0}, \tag{3.7}$$

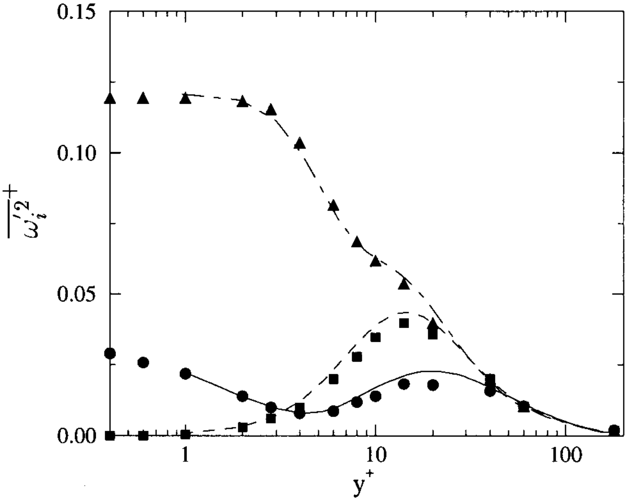

Figure 21. Distributions of the three components of mean square vorticity in wall units. Lines represent the current DNS results, and solid symbols the numerical data from KMM. — and ●, $\omega_x'^{2+}$; – – – and ▲, $\omega_y'^{2+}$; --- and ■, $\omega_z'^{2+}$.

$\tilde{y}$ refers to a co-ordinate measured in the cross-channel direction with an origin taken at the nearest wall, i.e. $\tilde{y} = L_y/2 - |y|$ using the present notations. τ_w is the mean shear stress at the wall; ρ_w is the mean density at the wall. The 'mean' operator mentioned in the previous definition refers to averaging in the spanwise and streamwise directions, and optionally in time. $\bar{u}(y)$ is the mean velocity profile. u_τ is called the wall shear velocity or friction velocity. The Reynolds number based on the wall shear velocity is defined as $Re_\tau = u_\tau h/\nu$. In the following, the superscript $+$ will be dedicated to normalized data in terms of wall units.

The present computation was conducted at the shear Reynolds number $Re_\tau = 180$, which corresponds to a convective Reynolds $Re_c = 3300$ (based on channel half-width and axial velocity). A mean centerline Mach number in the low-subsonic domain ($M = 0.2$) has been chosen. For this low Mach number flow, classical Reynolds space time averages can be used instead of Favre mass-weighted averages. The chosen conditions will also allow quantitative comparisons with the incompressible data of Kim *et al.* [7] at $Re_c = 3300$ (also noted KMM in the following) and to Wei and Willmarth [17] at $Re_c = 2970$ (also noted WW). Kim *et al.*'s channel flow data base [7] was also further explored to study the fine-scale structure of turbulence by Antonia *et al.* [19]. Some of the data presented here were taken from this last reference.

The computational grid contained $34 \times 121 \times 32$ points in the x-, y- and z-directions. The grid was uniform in the streamwise and spanwise directions, and the corresponding resolution was $\Delta_x^+ \simeq 33$ and $\Delta_z^+ \simeq 5$ in order to resolve the elongated structures of turbulence. In the cross-direction, a non-uniform mesh based on formula (2.18) was used, with constant C such that $\Delta_y^+ \simeq 1$ at the wall and $\Delta_y^+ \simeq 5$ near the centerline. It was obtained that $C = 1.120080625706$.

The initial conditions of the 3D computations are obtained using a random field superimposed to on 2D-saturated, linearly unstable mode at a higher Reynolds number. This two phase procedure greatly accelerates the convergence to a turbulent state. First, a 2D calculation is performed on a x–y subdomain of the 3D domain, using 34×121 points and the same mesh spacings. This 2D calculation is initialized with a laminar parabolic profile, on which a random velocity field (perturbation on u and v of amplitude 0.5% of the centerline velocity U_c) and a deterministic perturbation (most unstable mode taken from linear stability at $Re_c = 10000$ and for a domain of size $L_x \times L_y = 2\pi h \times 2h$, of amplitude 5%) are superimposed. It is noted that all 2D modes are linearly stable at $Re_c = 3300$. The evolution of the linear 2D mode is calculated at $Re_c = 10000$ and the simulation is stopped at a time before complete saturation. The obtained field is extended in the third direction (z) and a 3D random field is superimposed (perturbation on u, v and w of amplitude 0.75% of the centerline velocity U_c) in order to generate the 3D initial conditions. Non-linear modes start to grow from this initial condition, and a transition to a turbulent state is observed. After the transition, the 3D calculation must be conducted for a sufficiently long period so that the values of mean velocities and other statistics stabilize. Statistics are calculated by averaging in the x- and z-directions and time. Here, a time sample of roughly 140 convective time units (h/U_c) was used to get converged results.

3.3. Channel flow computations

In this section, the results obtained from the DNS presented in the previous sections will be discussed and compared to other data (numerical and experimental). All plots in wall unit co-ordinates correspond to an average between the lower and the upper wall profiles. This averaging operation can be omitted for perfectly converged results, which was nearly the case

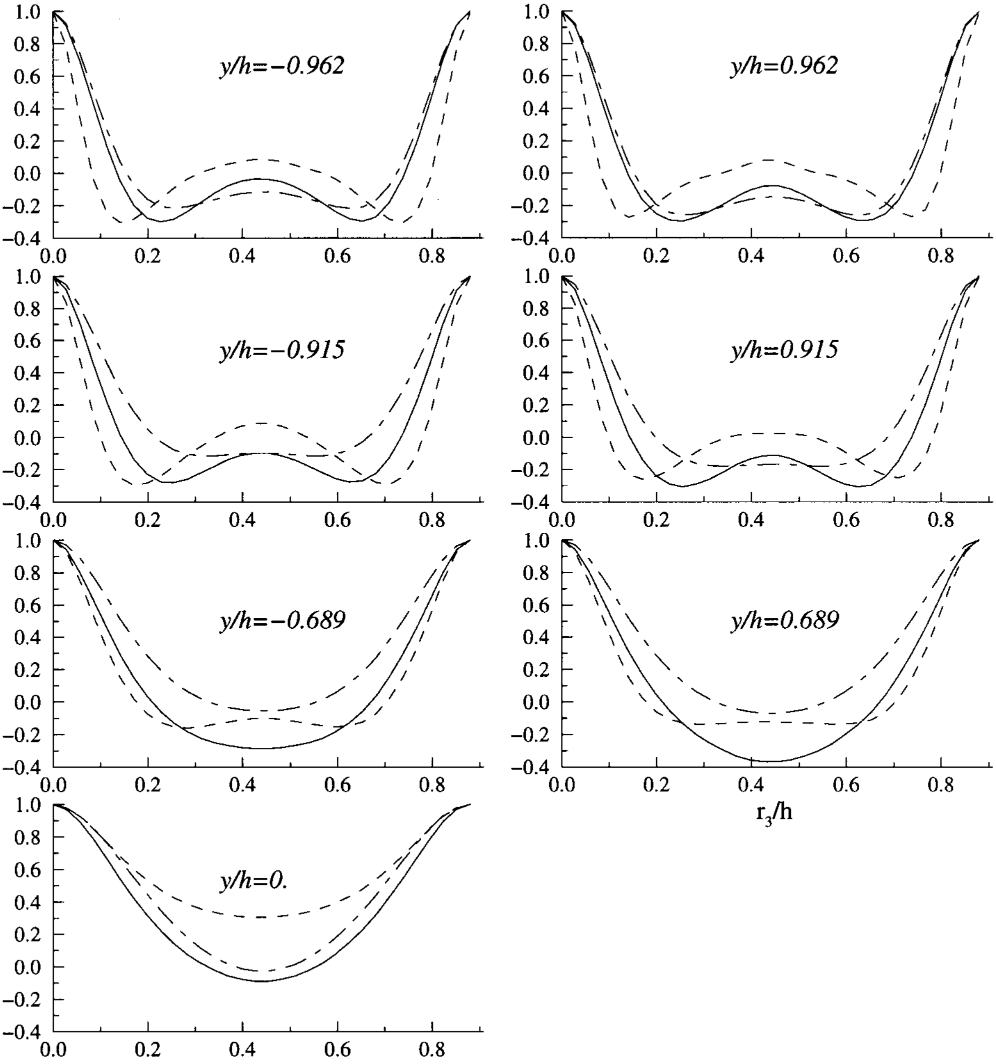

Figure 22. Spanwise two-point correlation functions. —, R_{11}; – – –, R_{22}; –·–, R_{33}.

here. Slight differences between the upper and lower wall profiles are, however, noticeable in the results, but these differences do not exceed a few percent (e.g 3, 4 and 5% on the $u^+_{\rm rms}$, $v^+_{\rm rms}$ and $w^+_{\rm rms}$ in Figure 17).

3.3.1. Mean velocity. The mean velocity profile normalized by the wall shear velocity is shown in Figure 16. The solid line shows the DNS results, and the symbols represent experimental data from WW at their convective Reynolds number $Re_{\rm c} = 2970$, which is the closest Reynolds number to the case considered here ($Re_{\rm c} = 3300$). Figure 16 also shows the law-of-the-wall plot compiled by Coles [21,22]. Note that the intercept value of 5.5 is used in the figure, and that the value found by the DNS results is a little overestimated. A linear sublayer can be seen, as well as a log layer for $y^+ > 30$. Results are comparable with the experimental data of WW.

3.3.2. Turbulence intensities. The mean-squared fluctuations of a given quantity q are computed by:

$$\overline{q'^2} = \overline{q^2} - (\bar{q})^2 \tag{3.8}$$

and root mean square (rms) fluctuations are defined by $q_{\rm rms} = \sqrt{\overline{q'^2}}$.

RMS velocity fluctuations normalized by the friction velocity are shown in Figure 17. Symbols represent data from other authors (see caption of Figure 17), while lines represent the present DNS results. Globally, both qualitative and quantitative trends are recovered by the present simulation. An underestimation of the streamwise velocity fluctuations $u^+_{\rm rms}$ is noticeable in Figure 17. However, a good qualitative agreement is observed between the present data and the experimental/numerical data of other authors: the peak of streamwise velocity

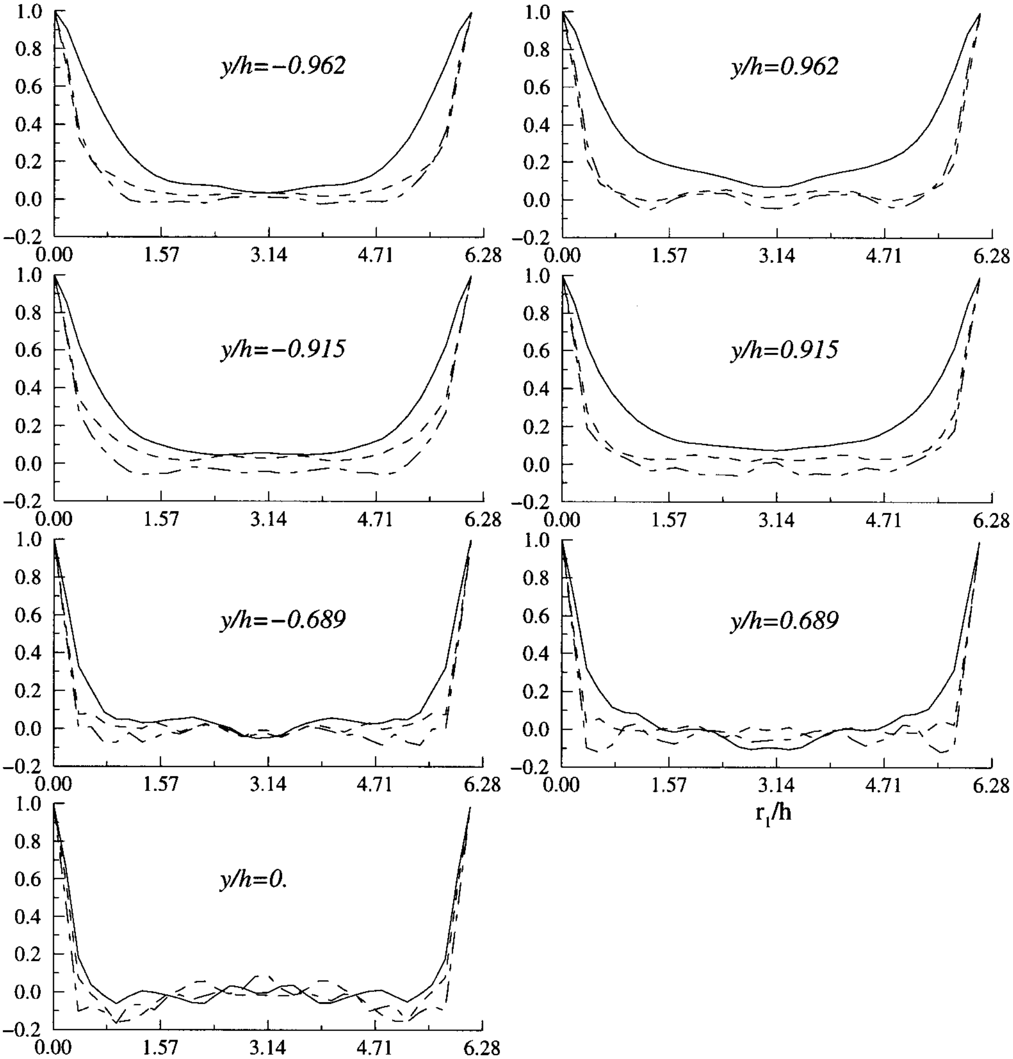

Figure 23. Streamwise two-point correlation functions. —, R_{11}; – – –, R_{22}; –·–, R_{33}.

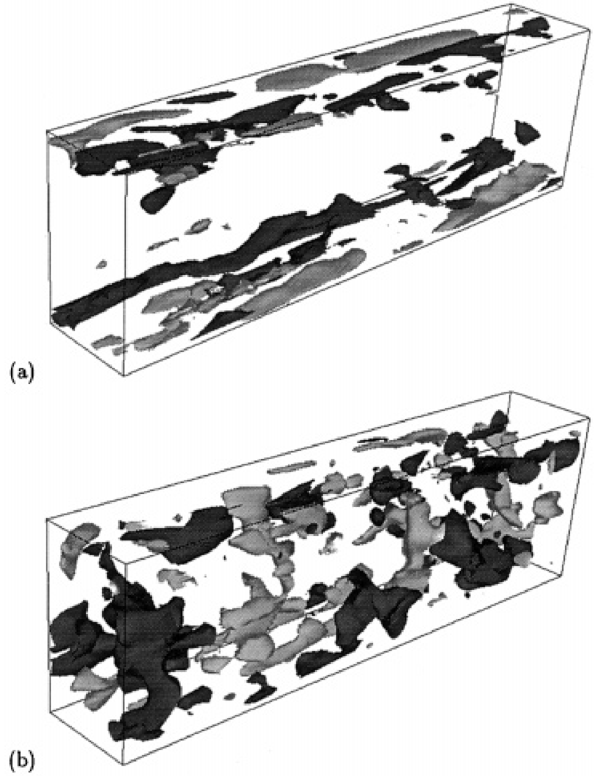

Figure 24. Instantaneous snapshots of velocity fluctuations: (a) isosurfaces $u'^{+} = \pm 2.875$; (b) isosurfaces $v'^{+} = \pm 1.15$. Negative isosurfaces, dark-grey; positive, light-grey.

fluctuations is obtained at $y^{+} = 13.2$, to be compared with the general experimentally admitted $y^{+} = 12$ value. Moreover, the data of KMM suggest a peak value at $y^{+} > 12$.

3.3.3. Shear stress. The total shear stress is given by (incompressible first-order approximation):

$$\tau_{\text{tot}} = \underbrace{-\overline{u'v'}}_{\text{Turbulent}} + \underbrace{\mu\left(\frac{\partial \bar{u}}{\partial y}\right)}_{\text{Linear}}. \tag{3.9}$$

The total shear stress written in wall units should be a linear function of the normal co-ordinate:

$$\tau^{+}_{\text{tot}} = 1 - \frac{y^{+}}{h^{+}}. \tag{3.10}$$

Although there is a slight dissymmetry in the profiles, Figure 18 shows that the above relation is satisfied. The turbulent and laminar components of τ^{+}_{tot} are also plotted in Figure 18. The turbulent shear stress is comparable with the experimental results of WW at $Re_{\text{c}} = 2970$.

3.3.4. Dissipation and Kolmogorov length scale. The homogeneous dissipation rate of turbulent kinetic energy $\bar{\varepsilon}$ can be defined, in the most general case and in non-dimensional variables by:

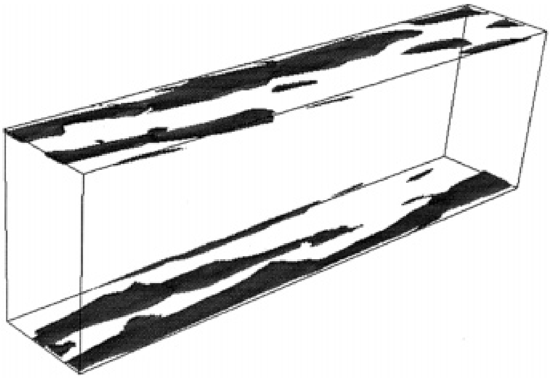

Figure 25. Instantaneous snapshot of vorticity magnitude. Isosurface $|\omega^+| = 1.11$.

$$\bar{\varepsilon} = \nu \overline{\frac{\partial u_i'}{\partial x_j}\left(\frac{\partial u_i'}{\partial x_j} + \frac{\partial u_j'}{\partial x_i}\right)}, \tag{3.11}$$

where repeated indices imply summation. The velocity instantaneous fluctuations are defined by:

$$u_i'(x, y, z, t) = u_i(x, y, z, t) - \overline{u_i}(y). \tag{3.12}$$

In direct simulations, the dissipation $\bar{\varepsilon}$ is expected to be strongly related to high frequency modes. Figure 19 shows the distribution of $\bar{\varepsilon}^+ = \bar{\varepsilon}\nu/u_\tau^4$ in wall co-ordinates. Symbols representing the numerical data of KMM are shown on the same plot. The same trend is observed between the two curves. A local peak is observed near $y^+ \approx 12$. Some discrepancies are, however, noticeable at low y^+. A lower resolution in the linear sublayer has been used here, compared with the KMM simulation. This could explain the observed discrepancies on $\bar{\varepsilon}^+$, since this quantity involves derivatives calculated on a coarser grid in the present simulation.

The Kolmogorov length scale $\eta_k = (\bar{\nu}^3/\bar{\varepsilon})^{1/4}$ is a measure of the characteristic size of the flow structures, at which the viscous dissipation of turbulent kinetic energy occurs. Figure 20 shows a plot of η_k^+ in wall unit co-ordinates. Results can be compared with the numerical data of KMM. It can be seen that η_k^+ is nearly constant in the wall region and increases in the outer region. The error between the two sets is nearly 12% near the centerline, while the data are similar elsewhere.

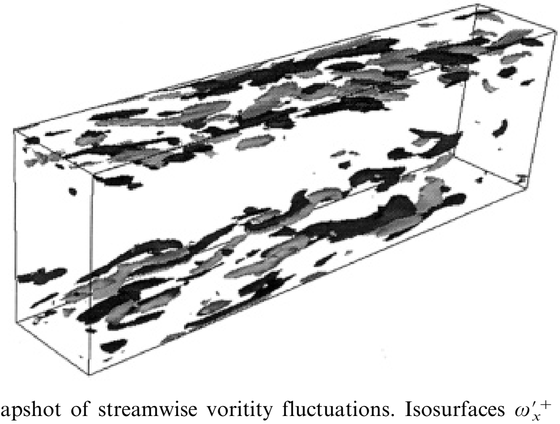

Figure 26. Instantaneous snapshot of streamwise voritity fluctuations. Isosurfaces $\omega_x'^+ = \pm 0.222$. (Negative, dark-grey; positive, light-grey).

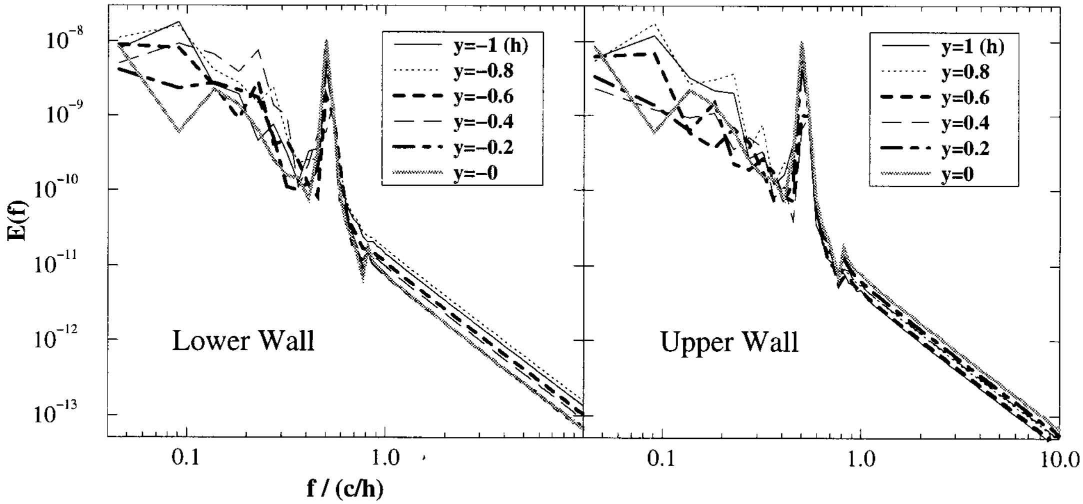

Figure 27. Temporal spectra of pressure signals recorded along the line $x_0 = 0$, $z_0 = 0$. Left: pressure probes closer to the lower wall; right: pressure probes closer to the upper wall. Notice the emergence of a particular frequency ($f = 0.5c/h$).

3.3.5. Vorticity distribution. The perturbation vorticity components are defined by $\omega'_i(x, y, z, t) = \omega_i(x, y, z, t) - \overline{\omega_i}$. The three components $\overline{\omega'^2_i}$ of the mean square perturbation vorticity are shown in Figure 21 in wall unit co-ordinates ($\omega^+ = \omega v/u_\tau^2$). In the same figure, the numerical data from KMM are also plotted. In this figure, it is observed that the distributions of the three components of vorticity are following the same trends as those of the numerical data from KMM, both qualitatively and quantitatively.

3.3.6. Turbulent flow structure and visualizations. A rapid analysis of the detailed structure of the computed flow field can be used to verify its validity. A more detailed analysis of flow structures in turbulent channel flows can be found in Moin and Kim [18].

The present computation should have sufficient grid resolution for the formation of the wall-layer streaks. The streaks are observed experimentally to have a mean spacing of $\Delta_z^+ \simeq 100$. The calculation of the two-point correlation functions is a good investigating tool:

$$\begin{aligned} R_{ii}(y, r_1) &= \frac{\overline{u'_i(x, y, z)u'_i(x + r_1, y, z)}}{\overline{u'^2_i(x, y, z)}} \\ R_{ii}(y, r_3) &= \frac{\overline{u'_i(x, y, z)u'_i(x, y, z + r_3)}}{\overline{u'^2_i(x, y, z)}} \end{aligned} \tag{3.13}$$

for $i = 1, 2, 3$ (no summation). Here, the averaging operator refers to an average in space (x- and z-directions) and time.

Figures 22 and 23 show respectively, the spanwise and streamwise correlation functions plotted at four different vertical locations. In all cases, the plots show both halves of the computational domain. The data are symmetric, which is a consequence of periodicity in those directions. Correlations were not computed during the simulation but were post-processed and averaged in time using only ten equally spaced ‘images’ of the flow field. This procedure seems sufficient to give global trends and converged results.

The spanwise correlation profiles show that negative minima occur for y-locations near the wall. The observed minimum is at $r_3^+ \approx 50$ for both $R_{11}(y, r_3)$ and $R_{33}(y, r_3)$, and at $r_3^+ \approx 25$ for $R_{22}(y, r_3)$. The separation at which $R_{11}(y, r_3)$ is minimum provides an estimate of the mean separation between the high- and low-speed fluid. The mean spacing between the streaks should be roughly twice the distance, which corresponds to experimental observations mentioned above. The presence of a minimum for $R_{22}(y, r_3)$ is consistent with the existence of streamwise vortical structures in the wall region. All these results are consistent with the observations of Kim *et al.* [7].

The streamwise correlation profiles show a slow decay of $R_{11}(y, r_1)$ for increasing r_1 near the wall. This clearly indicates that the eddies are highly elongated in the streamwise direction. Comparisons between $R_{11}(y, r_3)$ and $R_{11}(y, r_1)$ show that the spanwise extent of the structures is much smaller than their streamwise extent.

The instantaneous snapshots in Figures 24–26 show respectively, isosurfaces of velocity fluctuations, vorticity magnitude and streamwise vorticity fluctuations. Elongated eddies in the streamwise direction are also clearly visible on those instantaneous images.

3.3.7. Acoustics in the simulation. In the previous paragraphs, high- and low-order aerodynamic statistics are presented. These statistics do not mention the question of acoustics in the channel flow. This point is however, an interesting issue since, using periodic and isothermal wall boundary conditions in the simulation, *any acoustic perturbation generated will remain*

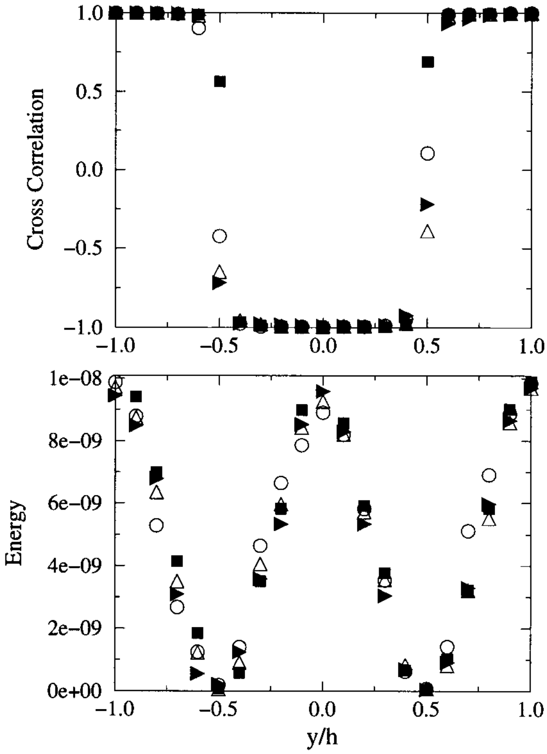

Figure 28. Pressure signals analysis. Bottom: spectral energy at frequency $f = 0.5c/h$ along cross-channel lines in the domain. Top: cross-correlations at frequency $f = 0.5c/h$ between the signal on the lower wall and the signals along cross-channel lines in the domain, showing relative phase information. Symbols refer to four different cross-channel lines at: ■, $x_0 = 0$ and $z_0 = 0$; ○, $x_0 = 0$ and $z_0 = L_z/2$; △, $x_0 = L_x/2$ and $z_0 = 0$; ▶, $x_0 = L_x/2$ and $z_0 = L_z/2$.

trapped in the computational domain. This question of acoustics has been poorly investigated in the literature, except in the work of Coleman [23,24] on DNS of isothermal wall supersonic channel flow, where compressible effects are much more important than in the present case. In the following, analysis will be based on Fourier transforms and spectral cross-correlations of signals recorded in the computational domain. This will allow the extraction of detailed information on the structure of acoustic modes in the presented simulation. For this purpose, numerical probes are placed at well-chosen locations in the domain, along four distinct cross-channel lines (i.e. lines in the y-direction), admitting the following projections in the x–z plane composed by the bottom wall: $x_0 = 0$ and $z_0 = 0$; $x_0 = 0$ and $z_0 = L_z/2$; $x_0 = L_x/2$ and $z_0 = 0$; $x_0 = L_x = /2$ and $z_0 = L_z/2$.

Time-Fourier averaged spectra of the pressure signals are plotted in Figure 27. These signals are recorded along the probe line $x_0 = 0$ and $z_0 = 0$ at a time near $t = 290h/U_c$. Energy refers to the normalized pressure spectral energy as:

$$E_p(f) = \left(\frac{|\hat{p}(f)|}{\rho_\omega c^2}\right)^2, \tag{3.14}$$

where $\hat{p}(f)$ is the Fourier transform of a pressure signal $p(t)$, and c is the mean speed of sound (based on wall temperature). In Figure 27, the emergence of a particular frequency: $f = 0.5c/h$, is clearly observed The same conclusion holds for any other line of probes.

A further analysis of the modal shape at this particular frequency is shown in Figure 28. This analysis was conducted at a time when the peak at $f = 0.5c/h$ could be reported (see next paragraph). The bottom of this figure shows the energy of the mode at $f = 0.5c/h$ as a function of y. Energy is maximal on the walls and at the center of the domain, and minimal at $y = \pm 0.5h$. The top part of Figure 28 shows relative phase information, obtained through Fourier cross-correlations of signals (the reference signal being the signal on the bottom wall). If $s_1(t)$ and $s_2(t)$ are temporal signals, and $\hat{s}_1(f)$ and $\hat{s}_2(f)$ their Fourier transforms, the cross-correlation of these signals in Fourier space, $\hat{C}_{12}(f)$, is calculated by:

$$\hat{C}_{12}(f) = \frac{\hat{s}_1(f)\hat{s}_2^{\dagger}(f)}{|\hat{s}_1(f)||\hat{s}_2(f)|}, \tag{3.15}$$

where the † symbol designates the complex conjugate. From Figure 28, it can be seen that, in regions situated close to the walls, the signals are in phase with respect to the lower wall (the correlation equals $+1$). On the other hand, near the centerline, the pressure signals have the opposite phases of the reference (bottom wall) signal (the correlation goes to -1). Thus, in this modal structure, the amplitude and phase characteristics of the second acoustic transverse mode ca be recognized.

The same analysis can be conducted at different times in the simulation. The second acoustic transverse mode can not be observed at the beginning of the simulation. After the transition, the mode is amplified. The amplification factor can be roughly estimated to $\alpha = 0.00547(U_c/h)$ (where $E(f, t) = E_0(f)\exp(2\alpha t)$ and $E(f, t)$ is the spectral energy at pressure antipodes). It now appears clear that acoustics take energy from the mean and turbulent motion. The turbulence structures (see Figures 24–26) excite the second acoustic transverse mode. However, this acoustic mode has *no effect* on the statistics, since the results shown in the previous sections are in good agreement with other incompressible numerical and experimental data.

4. CONCLUSION

In this paper, the development of a fourth-order (respectively third-order) compact scheme for the approximation of first (respectively second) derivatives on non-uniform meshes is proposed, by a full inclusion of metrics in the numerics of the compact scheme. The method is briefly compared with the classical methods using the JT, showing the advantages of the FIM method over the JT method for non-smoothly varying meshes.

An analysis of the numerical scheme is presented. A numerical analysis of truncation errors allows the recovery of the expected order of the scheme. A Fourier analysis completed by stability calculations in terms of both semi- and fully-discrete eigenvalue problems is also presented. In those eigenvalue problems, the constant speed convective equation is considered for the first derivative scheme analysis. On the other hand, the pure diffusion equation with a constant coefficient is considered for the analysis of the second derivative scheme. These eigenvalue computations show that the considered schemes are stable.

An application to the direct numerical simulation of compressible turbulent channel flow is then presented. The results of this simulation are compared with both experimental and other numerical (DNS) data in the literature. For the present DNS conditions, it is also reported that the second acoustic transverse mode is excited by turbulence, but that it has a negligible effect on turbulence statistics. Thus, the ability of the non-uniform mesh generalization of compact schemes to reproduce these physical results is demonstrated.

APPENDIX A. APPROXIMATION OF DERIVATIVES

The general solution for fourth-order, first derivative scheme on non-uniform meshes, with α_i and β_i parameters, is given by:

$$A_i = \frac{\begin{bmatrix} h_{i-1}h_ih_{i+1} + h_i^2h_{i+1} + h_{i-1}h_ih_{i+2} + h_i^2h_{i+2} - h_{i-1}h_i^2\alpha_i - h_{i-1}h_ih_{i+1}\alpha_i \\ -h_{i-1}h_ih_{i+2}\alpha_i - h_{i-1}h_ih_{i+1}\beta_i - h_i^2h_{i+1}\beta_i - h_{i-1}h_{i+1}^2\beta_i - 2h_ih_{i+1}^2\beta_i - h_{i+1}^3\beta_i \\ +h_{i-1}h_ih_{i+2}\beta_i + h_i^2h_{i+2}\beta_i + 2h_{i-1}h_{i+1}h_{i+2}\beta_i + 4h_ih_{i+1}h_{i+2}\beta_i + 3h_{i+1}^2h_{i+2}\beta_i \end{bmatrix}}{h_{i+1}(h_i + h_{i+1})(h_{i-1} + h_i + h_{i+1})h_{i+2}}, \tag{A.1}$$

$$B_i = \frac{\begin{bmatrix} -h_{i-1}h_{i+1}^2 - h_ih_{i+1}^2 - h_{i-1}h_{i+1}h_{i+2} - h_ih_{i+1}h_{i+2} - 3h_{i-1}h_i^2\alpha_i - 4h_{i-1}h_ih_{i+1}\alpha_i \\ +h_i^3\alpha_i + 2h_i^2h_{i+1}\alpha_i - h_{i-1}h_{i+1}^2\alpha_i + h_ih_{i+1}^2\alpha_i - 2h_{i-1}h_ih_{i+2}\alpha_i - h_{i-1}h_{i+1}h_{i+2}\alpha_i \\ +h_i^2h_{i+2}\alpha_i + h_ih_{i+1}h_{i+2}\alpha_i + h_{i-1}h_{i+1}h_{i+2}\beta_i + h_ih_{i+1}h_{i+2}\beta_i + h_{i+1}^2h_{i+2}\beta_i \end{bmatrix}}{h_{i-1}h_i(h_i + h_{i+1})(h_i + h_{i+1} + h_{i+2})}, \tag{A.2}$$

$$C_i = \frac{\begin{bmatrix} -h_{i-1}h_ih_{i+1} - h_i^2h_{i+1} + h_{i-1}h_i^2\alpha_i + h_{i-1}h_ih_{i+1}\alpha_i + h_{i-1}h_ih_{i+1}\beta_i + h_i^2h_{i+1}\beta_i \\ +h_{i-1}h_{i+1}^2\beta_i + 2h_ih_{i+1}^2\beta_i + h_{i+1}^3\beta_i \end{bmatrix}}{h_{i+2}(h_{i+1} + h_{i+2})(h_i + h_{i+1} + h_{i+2})(h_{i-1} + h_i + h_{i+1} + h_{i+2})}, \tag{A.3}$$

$$D_i = \frac{\begin{bmatrix} h_ih_{i+1}^2 + h_ih_{i+1}h_{i+2} - h_i^3\alpha_i - 2h_i^2h_{i+1}\alpha_i - h_ih_{i+1}^2\alpha_i - h_i^2h_{i+2}\alpha_i - h_ih_{i+1}h_{i+2}\alpha_i \\ -h_ih_{i+1}h_{i+2}\beta_i - h_{i+1}^2h_{i+2}\beta_i \end{bmatrix}}{h_{i-1}(h_{i-1} + h_i)(h_{i-1} + h_i + h_{i+1})(h_{i-1} + h_i + h_{i+1} + h_{i+2})}, \tag{A.4}$$

$$E_i = -(A_i + B_i + C_i + D_i). \tag{A.5}$$

For the first derivative, it is noticed that A_i, B_i, C_i, D_i and E_i are of the order $O(1/h_i)$.

The general solution for third-order second derivative, with α_i and β_i parameters, is given by:

$$A_i = \frac{2 \times \begin{bmatrix} -h_{i-1}h_i - h_i^2 + h_{i-1}h_{i+1} + 2h_i h_{i+1} + h_{i-1}h_{i+2} + 2h_i h_{i+2} + 2h_{i-1}h_i\alpha_i - h_i^2\alpha_i \\ +h_{i-1}h_{i+1}\alpha_i - h_i h_{i+1}\alpha_i + h_{i-1}h_{i+2}\alpha_i - h_i h_{i+2}\alpha_i - h_{i-1}h_i\beta_i - h_i^2\beta_i \\ -2h_{i-1}h_{i+1}\beta_i - 4h_i h_{i+1}\beta_i - 3h_{i+1}^2\beta_i + h_{i-1}h_{i+2}\beta_i + 2h_i h_{i+2}\beta_i + 3h_{i+1}h_{i+2}\beta_i \end{bmatrix}}{h_{i+1}h_{i+2}(h_i + h_{i+1})(h_{i-1} + h_i + h_{i+1})}, \tag{A.6}$$

$$B_i = \frac{2 \times \begin{bmatrix} 2h_{i-1}h_{i+1} + 2h_i h_{i+1} - h_{i+1}^2 + h_{i-1}h_{i+2} + h_i h_{i+2} - h_{i+1}h_{i+2} + 2h_{i-1}h_{i+1}\alpha_i \\ -3h_i^2\alpha_i + 3h_{i-1}h_i\alpha_i - 4h_i h_{i+1}\alpha_i - h_{i+1}^2\alpha_i + h_{i-1}h_{i+2}\alpha_i - 2h_i h_{i+2}\alpha_i - h_i h_{i+1}\beta_i \\ -h_{i-1}h_{i+1}\beta_i - h_{i+1}h_{i+2}\alpha_i - h_{i+1}^2\beta_i + h_{i-1}h_{i+2}\beta_i + h_i h_{i+2}\beta_i + 2h_{i+1}h_{i+2}\beta_i \end{bmatrix}}{h_{i-1}h_i(h_i + h_{i+1})(h_i + h_{i+1} + h_{i+2})}, \tag{A.7}$$

$$C_i = \frac{2 \times \begin{bmatrix} h_{i-1}h_i + h_i^2 - h_{i-1}h_{i+1} - 2h_i h_{i+1} - 2h_{i-1}h_i\alpha_i + h_i^2\alpha_i - h_{i-1}h_{i+1}\alpha_i \\ + h_i h_{i+1}\alpha_i + h_{i-1}h_i\beta_i + h_i^2\beta_i + 2h_{i-1}h_{i+1}\beta_i + 4h_i h_{i+1}\beta_i + 3h_{i+1}^2\beta_i \end{bmatrix}}{h_{i+2}(h_{i+1} + h_{i+2})(h_i + h_{i+1} + h_{i+2})(h_{i-1} + h_i + h_{i+1} + h_{i+2})}, \tag{A.8}$$

$$D_i = \frac{2 \times \begin{bmatrix} -2h_i h_{i+1} + h_{i+1}^2 - h_i h_{i+2} + h_{i+1}h_{i+2} + 3h_i^2\alpha_i + 4h_i h_{i+1}\alpha_i + h_{i+1}^2\alpha_i \\ + 2h_i h_{i+2}\alpha_i + h_{i+1}h_{i+2}\alpha_i + h_i h_{i+1}\beta_i + h_{i+1}^2\beta_i - h_i h_{i+2}\beta_i - 2h_{i+1}h_{i+2}\beta_i \end{bmatrix}}{h_{i-1}(h_{i-1} + h_i)(h_{i-1} + h_i + h_{i+1})(h_{i-1} + h_i + h_{i+1} + h_{i+2})}, \tag{A.9}$$

$$E_i = -(A_i + B_i + C_i + D_i). \tag{A.10}$$

For the second derivative, it is noted that A_i, B_i, C_i, D_i and E_i are proportional to $O(1/h_i^2)$.

For non-periodic boundaries, the above formulae are no longer valid for points close to the boundaries. Non-centered approximations of lower-order developed in Appendix B must be applied instead.

APPENDIX B. BOUNDARY SCHEME FOR NON-UNIFORM MESHES

The first derivative at boundary point $i = 1$ is calculated from Equation (2.9). Equalizing the Taylor series coefficients up to third-order leads to a linear system of equations, from which α, A, B and C at $i = 1$ can be obtained:

$$\begin{aligned} A &= -\frac{3h_2 + 2h_3}{h_2(h_2 + h_3)} \\ B &= \frac{(h_2 + h_3)(2h_3 - h_2)}{h_2 h_3^2} \\ C &= \frac{h_2^2}{h_3^2(h_2 + h_3)} \\ \alpha &= \frac{h_2 + h_3}{h_3} \end{aligned} \tag{B.1}$$

At boundary point $i = 2$, a fourth-order matching in Equation (2.10) gives:

$$\begin{aligned}
A &= -\frac{2h_3^2(2h_2 + h_3)}{h_2(h_2 + h_3)^3} \\
B &= \frac{2(h_3 - h_2)}{h_2h_3} \\
C &= \frac{2h_2^2(h_2 + 2h_3)}{h_3(h_2 + h_3)^3} \\
\alpha &= \frac{h_3^2}{(h_2 + h_3)^2} \\
\beta &= \frac{h_2^2}{(h_2 + h_3)^2}
\end{aligned} \tag{B.2}$$

The second derivative at boundary point $i = 1$ is calculated from Equation (2.14). Equalizing the Taylor series coefficients up to second-order leads to a linear system of equations, from which A, B, C and D at $i = 1$ can be obtained:

$$\begin{aligned}
A &= \frac{2(3h_2 + 2h_3 + h_4 + 2h_3\alpha + h_4\alpha)}{h_2(h_2 + h_3)(h_2 + h_3 + h_4)} \\
B &= -\frac{2(2h_2 + 2h_3 + h_4 - h_2\alpha + 2h_3\alpha + h_4\alpha)}{h_2h_3(h_3 + h_4)} \\
C &= \frac{2(2h_2 + h_3 + h_4 - h_2\alpha + h_3\alpha + h_4\alpha)}{h_3(h_2 + h_3)h_4} \\
D &= -\frac{2(2h_2 + h_3 - h_2\alpha + h_3\alpha)}{h_4(h_3 + h_4)(h_2 + h_3 + h_4)}
\end{aligned} \tag{B.3}$$

At boundary point $i = 2$, a second-order matching in Equation (2.15) gives:

$$\begin{aligned}
A &= \frac{2(2h_3 + h_4 + 3h_2\alpha + 2h_3\alpha + h_4\alpha - h_3\beta + h_4\beta)}{h_2(h_2 + h_3)(h_2 + h_3 + h_4)} \\
B &= -\frac{2(2h_3 - h_2 + h_4 + 2h_2\alpha + 2h_3\alpha + h_4\alpha - h_2\beta - h_3\beta + h_4\beta)}{h_2h_3(h_3 + h_4)} \\
C &= \frac{2(-h_2 + h_3 + h_4 + 2h_2\alpha + h_3\alpha + h_4\alpha - h_2\beta - 2h_3\beta + h_4\beta)}{h_3(h_2 + h_3)h_4} \\
D &= \frac{2(h_2 - h_3 - 2h_2\alpha - h_3\alpha + h_2\beta + 2h_3\beta)}{h_4(h_3 + h_4)(h_2 + h_3 + h_4)}
\end{aligned} \tag{B.4}$$

REFERENCES

1. T. Passot and A. Pouquet, 'Numerical simulations of compressible homogeneous flows in the turbulent regime', *J. Fluid Mech.*, **181**, 441–466 (1987).
2. T.A. Zang, R.B. Dahlburg and J.P. Dahlburg, 'Direct and large-eddy simulations of three-dimensional compressible Navier–Stokes turbulence', *Phys. Fluid A*, **4**, 127–140 (1992).

3. S.T. Yu, L.S. Hultgren and N.S. Liu, 'Direct calculations of waves in fluid flows using high-order compact difference scheme', *AIAA J.*, **32**, 1766–1773 (1994).
4. M.M. Rai and P. Moin, 'Direct simulations of turbulent flow using finite difference schemes', *J. Comput. Phys.*, **96**, 15–53 (1991).
5. B.E. Mitchell, S.K. Lele and P. Moin, 'Direct computations of the sound generated by vortex pairing in an axisymmetric jet', *AIAA Paper 95–0504*, 1995.
6. S.K. Lele, 'Direct numerical simulations of compressible free shear flows', *AIAA Paper 89–0374*, 1989.
7. J. Kim, P. Moin and R.D. Moser, 'Turbulence statistics in fully developed channel flow at low Reynolds number', *J. Fluid Mech.*, **177**, 133–166 (1987).
8. S. Ghosal, 'An analysis of numerical errors in large eddy simulations of turbulence', *Tech. Rep. CTR-159*, Center for Turbulent Research, Stanford University, 1996.
9. A.G. Kravchenko and P. Moin, 'On the effect of numerical errors in large-eddy simulations of turbulent flows', *Tech. Rep. CTR-160*, Center for Turbulent Research, Stanford University, 1996.
10. F. Ducros, Simulations numériques directes et des grandes échelles de couches limites compressibles, *Ph.D. Thesis*, Institut de Mécanique de Grenoble, France, 1995.
11. S.K. Lele, 'Compact finite difference schemes with spectral-like resolution', *J. Comput. Phys.*, **103**, 16–42 (1992).
12. R. Vichnevetsky and J.B. Bowles, *Fourier Analysis of Numerical Approximations of Hyperbolic Equations*, SIAM, Philadelphia, PA, 1982.
13. A.B. Cain and R.H. Bush, 'Numerical wave propagation analysis for stretched grids', *AIAA Paper 94–0172*, 1994.
14. J. Laufer, 'Investigation of turbulent flow in a two-dimensional channel', *Tech. Rep. 1053*, NACA-Rep, 1951.
15. G. Comte-Bellot, Contribution à l'étude de la turbulence de conduite. *Ph.D. Thesis*, Université de Grenoble, France, 1963.
16. J.A. Clark, 'A study of incompressible turbulent boundary layers in channel flow', *Trans. ASME D: J. Basic Eng.*, **90**, 455 (1968).
17. T. Wei and W.W. Willmarth, 'Reynolds number effects on the structure of a turbulent channel flow', *J. Fluid Mech.*, **204**, 57–95 (1989).
18. P. Moin and J. Kim, 'Numerical investigation of turbulent channel flow', *J. Fluid Mech.*, **118**, 341–377 (1982).
19. R.A. Antonia, J. Kim and L.W.B. Browne, 'Some characteristics of small-scale turbulence in a turbulent duct flow', *J. Fluid Mech.*, **233**, 369–388 (1991).
20. J. Jimenez and P. Moin, 'The minimal flow unit in near-wall turbulence', *J. Fluid Mech.*, **225**, 213–240 (1991).
21. D. Coles, 'The law of the wake in the turbulent boundary layer', *J. Fluid Mech.*, **1**, 191–226 (1956).
22. D. Coles, 'Measurements in the boundary layer on a smooth flat plate in supersonic flow: Part I. the problem of the turbulent boundary layer', *Tech. Rep. 20–69*, JPL/Cal Tech Report, 1953.
23. G.N. Coleman, J. Kim and R.D. Moser, 'A numerical study of turbulent supersonic isothermal-wall channel flow', *J. Fluid Mech.*, **305**, 159–183 (1995).
24. G.N Coleman, 'Direct simulation of isothermal-wall supersonic channel flow', in *Annual Research Briefs*, pp. 313–328. Center for Turbulence Research, 1993.